

Giant Molecular clouds in RCW 106 (G333): Galactic mini-starbursts and massive star formation induced by supersonic cloud-cloud collisions

MIKITO KOHNO (河野樹人),^{1,2} RIN I. YAMADA (山田麟),² KENGO TACHIHARA (立原研悟),² SHINJI FUJITA (藤田真司),³ REI ENOKIYA (榎谷玲依),⁴ KAZUKI TOKUDA (徳田一起),^{5,6} ASAO HABE (羽部朝男),⁷ HIDETOSHI SANO (佐野栄俊),^{8,9} TAKAHIRO HAYAKAWA (早川貴敬),² FUMIKA DEMACHI (出町史夏),² TAKUTO ITO (伊藤拓冬),² KISETSU TSUGE (柘植紀節),^{8,10,11} ATSUSHI NISHIMURA (西村淳),¹² MASATO I.N. KOBAYASHI (小林将人),¹³ HIROAKI YAMAMOTO (山本宏昭),² AND YASUO FUKUI (福井康雄)²

¹Curatorial Division, Nagoya City Science Museum, 2-17-1 Sakae, Naka-ku, Nagoya, Aichi 460-0008, Japan

²Department of Physics, Graduate School of Science, Nagoya University, Furo-cho, Chikusa-ku, Nagoya, Aichi 464-8602, Japan

³Institute of Statistical Mathematics, 10-3 Midori-cho, Tachikawa, Tokyo, Japan

⁴Faculty of Science and Engineering, Kyushu Sangyo University, 2-3-1 Matsukadai, Fukuoka 813-8503, Japan

⁵Department of Earth and Planetary Sciences, Faculty of Sciences, Kyushu University, Fukuoka, Fukuoka 819-0395, Japan

⁶National Astronomical Observatory of Japan (NAOJ), National Institutes of Natural Sciences (NINS), 2-21-1 Osawa, Mitaka, Tokyo 181-8588, Japan

⁷Department of Physics, Faculty of Science, Hokkaido University, N10 W8, Kitaku, Sapporo, Hokkaido 060-0810, Japan

⁸Faculty of Engineering, Gifu University, 1-1 Yanagido, Gifu, Gifu 501-1193, Japan

⁹Center for Space Research and Utilization Promotion (c-SRUP), Gifu University, 1-1 Yanagido, Gifu 501-1193, Japan

¹⁰Institute for Advanced Study, Gifu University, 1-1 Yanagido, Gifu, Gifu 501-1193, Japan

¹¹Institute for Advanced Research, Nagoya University, Furo-cho, Chikusa-ku, Nagoya, Aichi 464-8601, Japan

¹²Nobeyama Radio Observatory, National Astronomical Observatory of Japan (NAOJ), National Institutes of Natural Sciences (NINS), 462-2, Nobeyama, Minamimaki, Minamisaku, Nagano 384-1305, Japan

¹³I. Physikalisches Institut Universität zu Köln Zùlpicher Straße 77 50937 Köln Germany

(Received 2024 November 15; Revised 2025 January 22; Accepted 2025 January 24)

ABSTRACT

To reveal the origin of the mini-starbursts in the Milky Way, we carried out large-scale CO observations toward the RCW 106 giant molecular cloud (GMC) complex using the NANTEN2 4-m radio telescope operated by Nagoya University. We also analyzed the Mopra Southern Galactic plane CO survey and Herschel infrared continuum archival data. The RCW 106 GMC complex contains the radial velocity components of -68 km s^{-1} and -50 km s^{-1} reported by [Nguyen et al. \(2015\)](#). Focusing on the RCW 106 East and West region with the massive star formation having the bright infrared dust emission, we found that these regions have three different velocity components with $\sim 10 \text{ km s}^{-1}$ differences. The two out of three velocity components show morphological correspondence with the infrared cold dust emission and connect with the bridge feature on a position-velocity diagram. Therefore, two molecular clouds (MCs) with $\sim 10 \text{ km s}^{-1}$ differences are likely to be physically associated with massive star-forming regions in the GMC complex. Based on these observational results, we argue that mini-starbursts and massive star/cluster formation in the RCW 106 GMC complex are induced by supersonic cloud-cloud collisions in an agglomerate of molecular gas on the Scutum-Centurus arm.

Keywords: Interstellar medium (847) — Giant molecular clouds (653) — Interstellar clouds (834) — Milky Way disk (1050) — Molecular gas (1073) — CO line emission (262)

1. INTRODUCTION

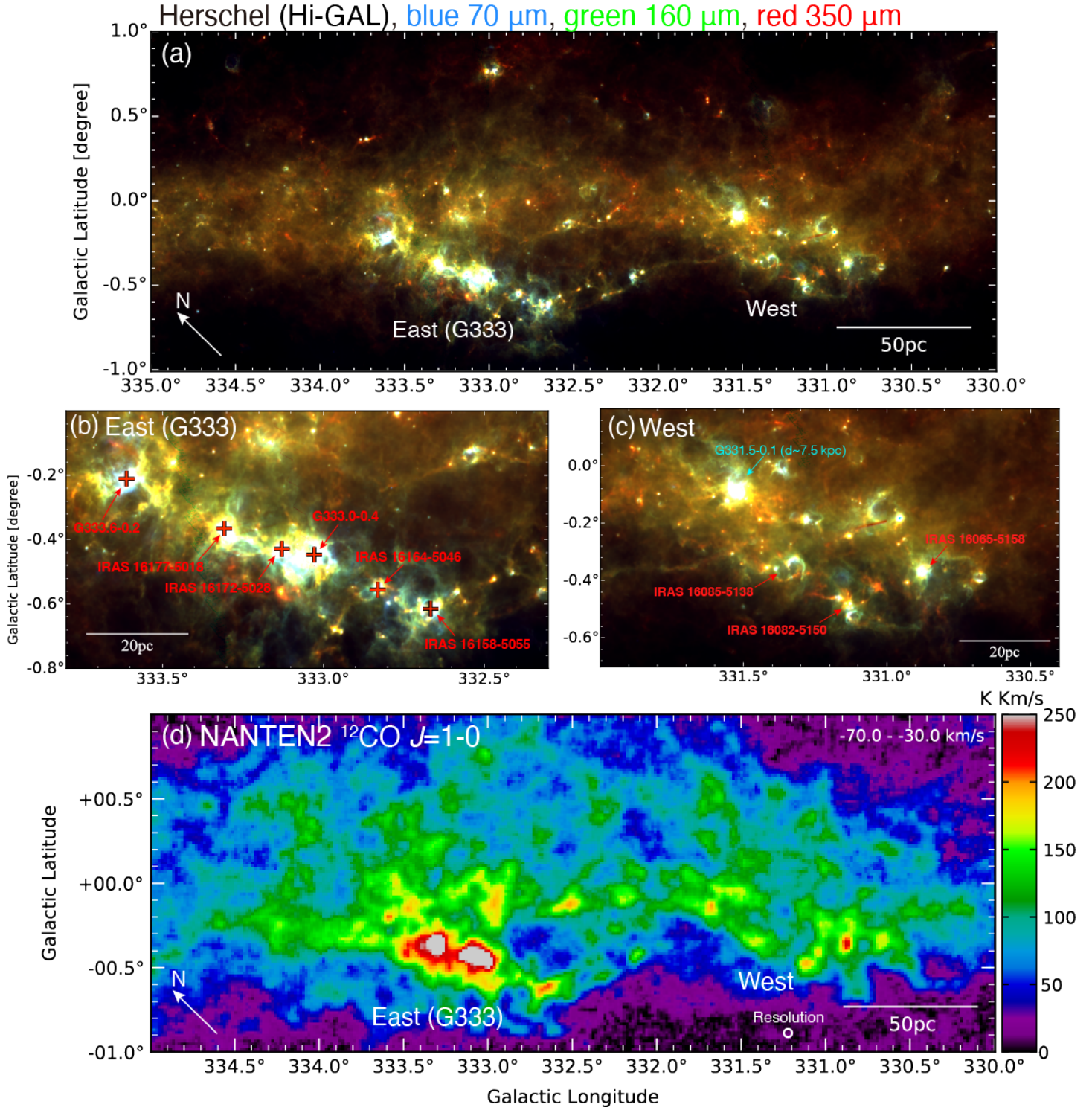


Figure 1. (a) The Herschel three-color composite image of the RCW 106 GMC complex. Blue, green, and red show the Herschel/PACS 70 μm , Herschel/PACS 160 μm , and Herschel/SPIRE 350 μm distributions, respectively (Molinari et al. 2016). (b) The Herschel close-up image of RCW 106 East (G333). The red cross marks are the positions of the massive star-forming regions in RCW 106 East (Bains et al. 2006). (c) The Herschel close-up image of RCW 106 West. (d) The NANTEN2 $^{12}\text{CO } J = 1-0$ integrated intensity map of the RCW 106 GMC complex. The integrated velocity range is from -70 km s^{-1} to -30 km s^{-1} .

Massive star formation is an essential topic in astrophysics because massive stars emit ultraviolet radiation and affect the surrounding interstellar medium. They are born as star clusters in giant molecular clouds (GMCs) on the Galactic disk (e.g., Lada & Lada 2003; Ascenso 2018; Krumholz et al. 2019; Krause et al. 2020). Extreme massive star formation in a GMC is known as mini-starburst regions in the Milky Way, which have been studied by multi-wavelength observations, for example, radio, infrared, optical ($H\alpha$), X-ray, and gamma ray (Nguyen Luong et al. 2011; Russeil et al. 2016; Fukui et al. 2018b; Motte et al. 2018; Yang & Wang 2020; Kohno et al. 2021; Pouteau et al. 2023; Sasaki et al. 2024; LHAASO Collaboration 2024).

RCW 106 (Rodgers et al. 1960) is the massive star-forming region associated with the Scutum-Centaurus arm at a kinematic distance of ~ 3.6 kpc from the solar system (Nguyen et al. 2015). This kinematic distance is calculated by the radial velocity of molecular gas using the Galactic rotation curve (Reid et al. 2009) and is also consistent with the spectrophotometric distance at the OB star cluster in RCW 106 (Moisés et al. 2011). The total molecular mass is $5.9 \times 10^6 M_{\odot}$ as one of the most massive molecular cloud complexes in the Milky Way (Nguyen et al. 2015; Nguyen-Luong et al. 2016). The RCW 106 GMC complex contains ~ 50 O-type stars (Nguyen et al. 2015) and has been studied as the mini-starburst region by infrared, optical ($H\alpha$), and radio observations (e.g., Gillespie et al. 1977; Karnik et al. 2001; Mookerjee et al. 2004; Russeil et al. 2005; Bains et al. 2006; Breen et al. 2007; Wong et al. 2008; Lo et al. 2009, 2011; Simpson et al. 2012; Lowe et al. 2014; Wiles et al. 2016; Tamaoki et al. 2019; Motte et al. 2022). Previous CO observations revealed that molecular clouds are composed of different radial velocities of -90 km s^{-1} , -64 km s^{-1} , and -48 km s^{-1} (Nguyen et al. 2015). The -90 km s^{-1} component is associated with the massive star-forming region G331.5-0.1 (MCC 331-90) at a distance of ~ 7.5 kpc in the Norma arm (Merello et al. 2013). Nguyen et al. (2015) suggest that the -64 km s^{-1} and -48 km s^{-1} components are associated with the RCW 106 GMC complex in the Scutum-Centaurus arm.

Figure 1(a) presents a three-color composite image obtained by the Herschel infrared Galactic Plane Survey (Hi-GAL). Blue, green, and red presents $70 \mu\text{m}$, $160 \mu\text{m}$, and $350 \mu\text{m}$ continuum image, respectively. These far-infrared image mainly trace cold dust components with the temperature of $10 < T < 40$ K (e.g., Molinari et al. 2010a).

RCW 106 complex has two bright regions in the infrared image, as shown in the close-up image in Figures 1(b) and 1(c); hereafter, we call RCW 106 East and RCW 106 West, respectively. RCW 106 East (G333) is the brightest region in the GMC complex and contains the massive cluster G333.6-0.2 (Becklin et al. 1973; Hyland et al. 1980; Fujiyoshi et al. 1998, 2001, 2005, 2006; Kumar 2013; Grave et al. 2014; Towner et al. 2024; Bonfand et al. 2024; Dell’Ova et al. 2024), massive star-forming region IRAS 16177-5018, IRAS 16172-5028 (=G333.1-0.4; Figuerêdo et al. 2005), G333.0-0.4 (Lo et al. 2015), IRAS 16164-5046 (=G332.8-0.6), and IRAS 16158-5055 (see Figure 3 in Bains et al. 2006). RCW 106 West includes massive star-forming regions of IRAS 16085-5138 (Pinheiro et al. 2012), IRAS 16082-5150, and IRAS 16065-5158 (Dedes et al. 2011). The region between RCW 106 East and RCW 106 West is the G332 region reported the filamentary structure (Romano et al. 2019). Recently, Zhou et al. (2023) performed large-scale ^{13}CO ($J = 3-2$) observations toward the RCW 106 GMC complex using the APEX/LAsMA heterodyne camera. They reported the hub-filament system in RCW 106 and suggested the state of global gravitational collapse (see also Zhou et al. 2024a,b). On the other hand, previous studies have not clarified the relation between two radial velocity components in the RCW 106 GMC complex and massive star/cluster formation. It has also been suggested that shock waves resulting from large-scale gas collisions are crucial in the formation of hub-filament systems (e.g., Inoue et al. 2018; Maity et al. 2024, 2025), and observationally, massive star-forming regions consistent with these predictions are being discovered (e.g., Fukui et al. 2019; Tokuda et al. 2019, 2022, 2023). Therefore, investigating the global gas kinematics in regions with hub-filamentary cloud candidates is becoming an urgent issue. RCW 106, which is one of the most massive complexes in the Galactic plane observable from the southern sky, is thus an optimal region for such research. In this paper, we aim to reveal the relation between the origin of massive star formation and different radial velocity components in the RCW 106 GMC complex.

This paper is structured as follows: section 2 introduces observations and the archival data; Section 3 shows the results; Section 4 discusses the massive cluster formation scenario in the RCW 106 GMC complex; and Section 5 summarizes this paper.

2. OBSERVATIONS AND ARCHIVAL DATA

2.1. NANTEN and NANTEN2 ^{12}CO $J = 1-0$ observations

Table 1. Observational data properties.

Telescope	Line	HPBW	Grid	Velocity Resolution	r.m.s noise* level	References
NANTEN	$^{12}\text{CO } J = 1-0$	2'6	4'	0.65 km s $^{-1}$	~ 0.2 K	[1,2]
NANTEN2	$^{12}\text{CO } J = 1-0$	2'6	1'	0.16 km s $^{-1}$	~ 1.1 K	
Mopra	$^{12}\text{CO } J = 1-0$	$\sim 33''$	30''	0.1 km s $^{-1}$	~ 0.8 K	[3,4,5,6]
	$^{13}\text{CO } J = 1-0$	$\sim 33''$	30''	0.1 km s $^{-1}$	~ 0.3 K	[3,4,5,6]

Telescope/Survey	Band	Detector	Resolution	Grid	References
Herschel/Hi-GAL	70 μm	PACS	$\sim 6''$	3''	[7,8]
Herschel/Hi-GAL	160 μm	PACS	$\sim 12''$	4.5''	[7,8]
Herschel/Hi-GAL	350 μm	SPIRE	$\sim 24''$	8''	[7,9]

Notes. *The r.m.s noise level is taken from the final cube data using this paper. References [1] Mizuno & Fukui (2004), [2] Takeuchi et al. (2010), [3] Burton et al. (2013), [4] Braiding et al. (2015) [5] Braiding et al. (2018) [6] Cubuk et al. (2023), [7] Molinari et al. (2010a) [8] Poglitsch et al. (2010), [9] Griffin et al. (2010)

We carried out the $^{12}\text{CO } J = 1-0$ survey observations toward the southern Galactic plane from March 2012 to December 2012 using the NANTEN2 radio telescope at Pampalabola in Chile. NANTEN2¹ has a diameter of 4 m, operated by Nagoya University. The half power beam width (HPBW) is 2'6 at 115.271 GHz, the rest frequency of $^{12}\text{CO } J = 1-0$. The observations were performed using the on-the-fly (OTF) mapping mode. We used the 4 K cooled superconductor-insulator-superconductor (SIS) receiver in the front-end system. The system noise temperature shows ~ 250 K at the double-sideband (DSB). The back-end system is a digital-Fourier-transform spectrometer (DFS) with a 1 GHz bandwidth and 16384 channels. The velocity bandwidth and resolution are 2600 km s $^{-1}$ and 0.16 km s $^{-1}$ at 115 GHz, respectively. Observers checked the pointing accuracy within 15'' by observing a variable carbon star IRC+10216 and the Sun. The raw data, including the atmosphere, is converted to the antenna temperature scale (T_A^*) by applying the chopper-wheel method (Ulich & Haas 1976; Kutner & Ulich 1981). We daily observed IRAS 16293–2422 ($\alpha_{\text{J2000}}, \delta_{\text{J2000}} = (16^{\text{h}}32^{\text{m}}23.3^{\text{s}}, -24^{\circ}28'39.''2)$) located in the Rho Ophiuchi star-forming region as a standard source. We calibrated T_A^* to the main-beam temperature scale (T_{MB}), assuming $T_{\text{MB}} = 18$ K (Ridge et al. 2006) as the peak intensity of IRAS 16293–2422. The cube data is smoothed to be 180'' spatial resolution using the kernel Gaussian function of 90''. The grid size of the final data is $(l, b, v) = (60'', 60'', 0.16 \text{ km s}^{-1})$. The root-mean-square (r.m.s.) noise level is ~ 1.1 K at T_{mb} scale. The current status of the NANTEN2 radio telescope is described in Nishimura et al. (2020).

We also used the $^{12}\text{CO } J = 1-0$ survey data from the NANTEN 4 m telescope at Las Campanas observatory in Chile until 2004. The detailed information of this data is described in Mizuno & Fukui (2004) and Takeuchi et al. (2010). The HPBW, grid spacing, and velocity resolution are 2'6, 4', and 0.65 km s $^{-1}$, respectively. The grid size and r.m.s noise level of cube data used in this paper are $(l, b, v) = (4', 4', 1 \text{ km s}^{-1})$ and ~ 0.2 K at T_{mb} scale.

2.2. The Mopra ^{12}CO and $^{13}\text{CO } J = 1-0$ Galactic Plane survey data

To perform a detailed analysis focusing on RCW 106 East and RCW 106 West, we utilized the high-resolution CO data obtained by the Mopra Southern Galactic Plane CO Survey (Burton et al. 2013; Braiding et al. 2015, 2018; Cubuk et al. 2023)². The Mopra radio telescope, with a diameter of 22 m, is operated by the Australia Telescope National Facility (ATNF). The Mopra Southern Galactic plane survey was observed in the ^{12}CO , ^{13}CO , C^{18}O , and $\text{C}^{17}\text{O } J = 1-0$ emission, carried out during the winter season from 2011 to 2018. The observations were the Fast-On-The-Fly (FOTF) mode every $60' \times 6'$ rectangle unit. The telescope performed orthogonal scans in the direction of Galactic longitude and latitude to reduce scanning artifacts. Part of the observations were conducted remotely from Nagoya University in Japan through an internet connection. The front end uses a Monolithic Microwave Integrated Circuit (MMIC) receiver covered with a 3 mm band. The back end is utilized as the UNSW Mopra Spectrometer (MOPS). The HPBW of Mopra at 115 GHz is 33''. The survey data is converted to the main-beam temperature scale using the relation of $T_{\text{MB}} = T_A^*/\eta$ with the extended beam efficiency of $\eta = 0.55$ (Ladd et al. 2005). The spatial and

¹ <https://www.a.phys.nagoya-u.ac.jp/jp/index.php/nanten2/>

² <https://mopracosurvey.wordpress.com>

velocity resolution of the data release 4 (DR4) is $36''$ and 0.1 km s^{-1} , respectively. The grid size used in this paper is $(l, b, v) = (30'', 30'', 1 \text{ km s}^{-1})$. The r.m.s noise levels are $\sim 0.8 \text{ K}$ in $^{12}\text{CO } J = 1-0$ and $\sim 0.3 \text{ K}$ in $^{13}\text{CO } J = 1-0$.

2.3. The Herschel far-infrared archival data

To compare spatial distributions between molecular gas and massive star/cluster sources in the RCW 106 GMC complex, we used the archival infrared image data obtained by Herschel Space Observatory³ (Pilbratt et al. 2010). The image data are taken from the VIALACTEA web page⁴ as a part of the Herschel infrared Galactic Plane Survey (Hi-GAL: Molinari et al. 2010a,b, 2016). The far-infrared image data of $70 \mu\text{m}$, $160 \mu\text{m}$, and $350 \mu\text{m}$ are obtained by the Photodetector Array Camera and Spectrometer (PACS: Poglitsch et al. 2010) and Spectral and Photometric Imaging REceiver (SPIRE: Griffin et al. 2010), respectively. The spatial resolution of $70 \mu\text{m}$, $160 \mu\text{m}$, and $350 \mu\text{m}$ data are $6''$, $12''$, and $24''$, respectively. Table 1 summarizes the data properties in this paper.

3. RESULTS

3.1. CO spatial and velocity distributions of the RCW 106 GMC complex

Figure 1(d) shows the $^{12}\text{CO } J = 1-0$ integrated intensity map obtained by NANTEN2. The molecular cloud distributes over $200 \text{ pc} \times 80 \text{ pc}$ ($l \times b$) at the Galactic plane from $l = 330^\circ$ to 335° . The CO peak has $(l, b) \sim (333.3, -0.35)$, which corresponds to the active massive star-forming of G333 including G333.6-0.2, IRAS 16177-5018, IRAS 16172-5028, G333.0-0.4, IRAS 16164-5046, and IRAS 16158-5055 (see Figure 3 of Bains et al. 2006). The CO peaks coincide with the bright infrared regions at RCW 106 East and RCW 106 West, as shown in Figures 1(a) and (d). Figure 2(a) presents the large-scale longitude-velocity diagram of $^{12}\text{CO } J = 1-0$ obtained by NANTEN. The two velocity components of -90 km s^{-1} and -50 km s^{-1} at $l \sim 333^\circ$ correspond to the Norma arm and Scutum-Centaurus arm in the Milky Way, respectively (Vallée 2017; Koda et al. 2016). The yellow dotted box shows the main components of the RCW 106 GMC complex. Figure 2(b) shows the detailed longitude-velocity diagram of $^{12}\text{CO } J = 1-0$, focusing on the RCW 106 GMC complex obtained by NANTEN2. In this figure, we can find two velocity components of $\sim -68 \text{ km s}^{-1}$ and $\sim -50 \text{ km s}^{-1}$ in the GMC complex. The CO gas has a peak at RCW 106 East. These two components are separated at RCW 106 West and connect on the velocity space with the bridge feature.

Figures 3 (a) and (b) show the $^{12}\text{CO } J = 1-0$ spectra in RCW 106 East and RCW 106 West, respectively. The positions of the spectra are shown as the orange cross marks in Figures 5a and 5b. Previous studies indicate that the velocity range from -110 km s^{-1} to -90 km s^{-1} is associated with the Norma arm with a distance of $\sim 4.6-7.5 \text{ kpc}$ and the background component toward RCW 106 (Merello et al. 2013; Nguyen et al. 2015). The velocity range from -80 km s^{-1} to -30 km s^{-1} is associated with RCW 106 located on the Scutum-Centaurus arm and is composed of two velocity components, which are from -75 km s^{-1} to -60 km s^{-1} and from -60 km s^{-1} to -40 km s^{-1} . Hereafter, we call these components “ -68 km s^{-1} GMC” and “ -50 km s^{-1} GMC”.

Figure 4 shows the velocity channel map of $^{12}\text{CO } J = 1-0$ from -80 km s^{-1} to -30 km s^{-1} . Molecular gas distributes from -70 km s^{-1} to -35 km s^{-1} . We can find the two filamentary structures in RCW 106 East and West from -53 km s^{-1} to -49 km s^{-1} . Their lengths and widths are $\sim 150 \text{ pc}$ and $\sim 20 \text{ pc}$ at a distance of 3.6 kpc . Previous studies identified these filaments as the giant molecular filament of GMF 335.6-333.6a and GMF 335.6-333.6b (Abreu-Vicente et al. 2016; Zucker et al. 2018; Zhang et al. 2019).

3.2. Two giant molecular clouds

Figures 5(a) and (b) display the $^{12}\text{CO } J = 1-0$ integrated intensity maps of the -68 km s^{-1} and -50 km s^{-1} GMC. The -68 km s^{-1} GMC exhibits a peak at RCW 106 West and a filamentary structure from North to South. The -50 km s^{-1} GMC elongates along the Galactic plane and peaks at RCW 106 East. We calculated the H_2 column densities and molecular masses within the range above the 5σ noise level with the ^{12}CO integrated intensity, assuming the CO-to- H_2 conversion factor of $2 \times 10^{20} \text{ cm}^{-2} (\text{K km s}^{-1})^{-1}$ (Bolatto et al. 2013). The peak H_2 column densities of the -68 km s^{-1} GMC and -50 km s^{-1} GMC are $3.3 \times 10^{22} \text{ cm}^{-2}$ and $5.7 \times 10^{22} \text{ cm}^{-2}$, respectively. The total molecular mass of -68 km s^{-1} GMC and -50 km s^{-1} GMC are $\sim 4.0 \times 10^6 M_\odot$ and $\sim 5.5 \times 10^6 M_\odot$, respectively. In the appendix, we present detailed procedures for derived physical properties of molecular clouds. Figures 6(a) and (b) show the -68 km s^{-1} and -50 km s^{-1} GMC superposed on the Herschel $160 \mu\text{m}$ dust continuum image (Molinari et

³ Herschel Space Observatory is an ESA space observatory with science instruments provided by European-led Principal Investigator consortia and with important participation from NASA.

⁴ <http://vialactea.iaps.inaf.it/vialactea/eng/index.php>

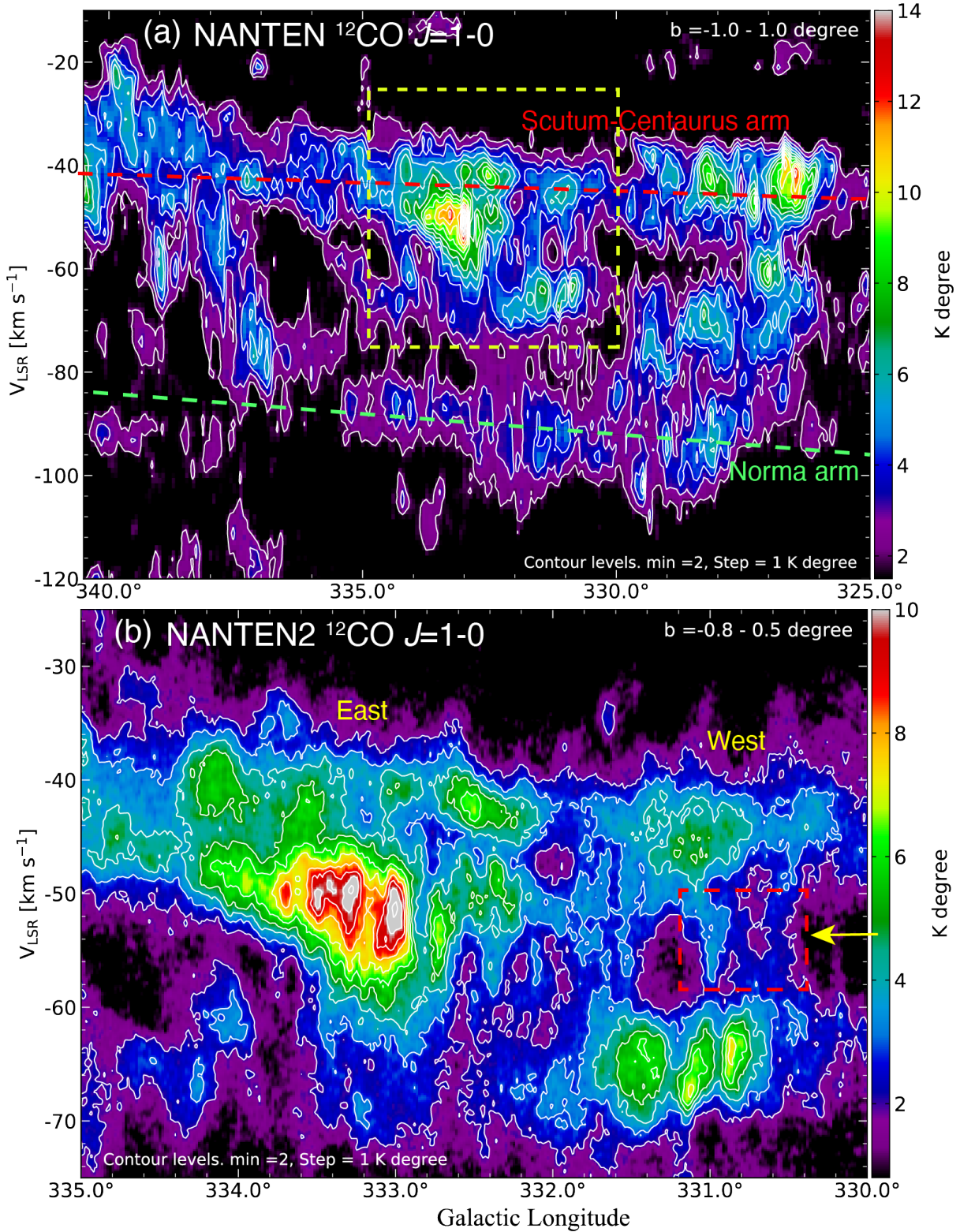


Figure 2. (a) The large-scale longitude-velocity diagram of $^{12}\text{CO } J = 1-0$ obtained by NANTEN. The red and green dotted lines indicate the Scutum-Centaurus and Norma arm, respectively (Vallée 2017; Koda et al. 2016). The integrated latitude range is from -1.0° to 1.0° . The yellow dotted square shows the area in panel (b). (b) Detailed longitude-velocity diagram focusing on the RCW 106 GMC complex of $^{12}\text{CO } J = 1-0$ obtained by NANTEN2. The integrated latitude range is from -0.8° to 0.5° . The red dotted rectangle and yellow arrow show the bridge feature at RCW 106 West. The velocity space is smoothed in 9 channels by the hanning window. The lowest contour and interval are 2 K degree and 1 K degree, respectively.

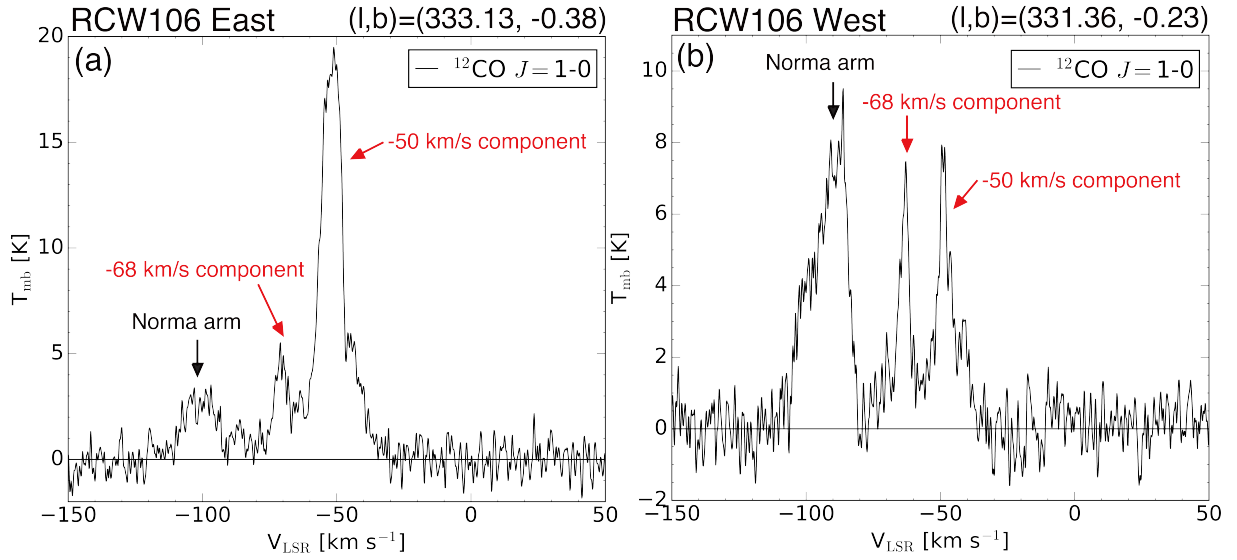


Figure 3. Spectra for $^{12}\text{CO } J = 1-0$ obtained at (a) RCW 106 East (G333), and (b) RCW 106 West with NANTEN2. The red arrows indicate the velocity components associated with the RCW 106 GMC complex. The black arrow shows the velocity component of the Norma arm. The spectra are smoothed to the velocity domain of 9 channels by the hanning window. The position of each spectrum is shown in the upper right of each panel and the orange cross marks in Figures 5a and 5b.

al. 2010a). We point out that peaks of molecular gas coincide with bright cold dust emission, as shown in the Herschel infrared image at RCW 106 East and RCW 106 West. These results indicate that the molecular clouds with a velocity difference of $\sim 20 \text{ km s}^{-1}$ are likely to be physically associated with the active star-forming regions in the RCW 106 GMC complex. Based on the large-scale observational results, we performed a detailed analysis focusing on RCW 106 East and RCW 106 West to reveal the relationship between two GMCs and massive star/cluster formation in the RCW 106 GMC complex in the next section.

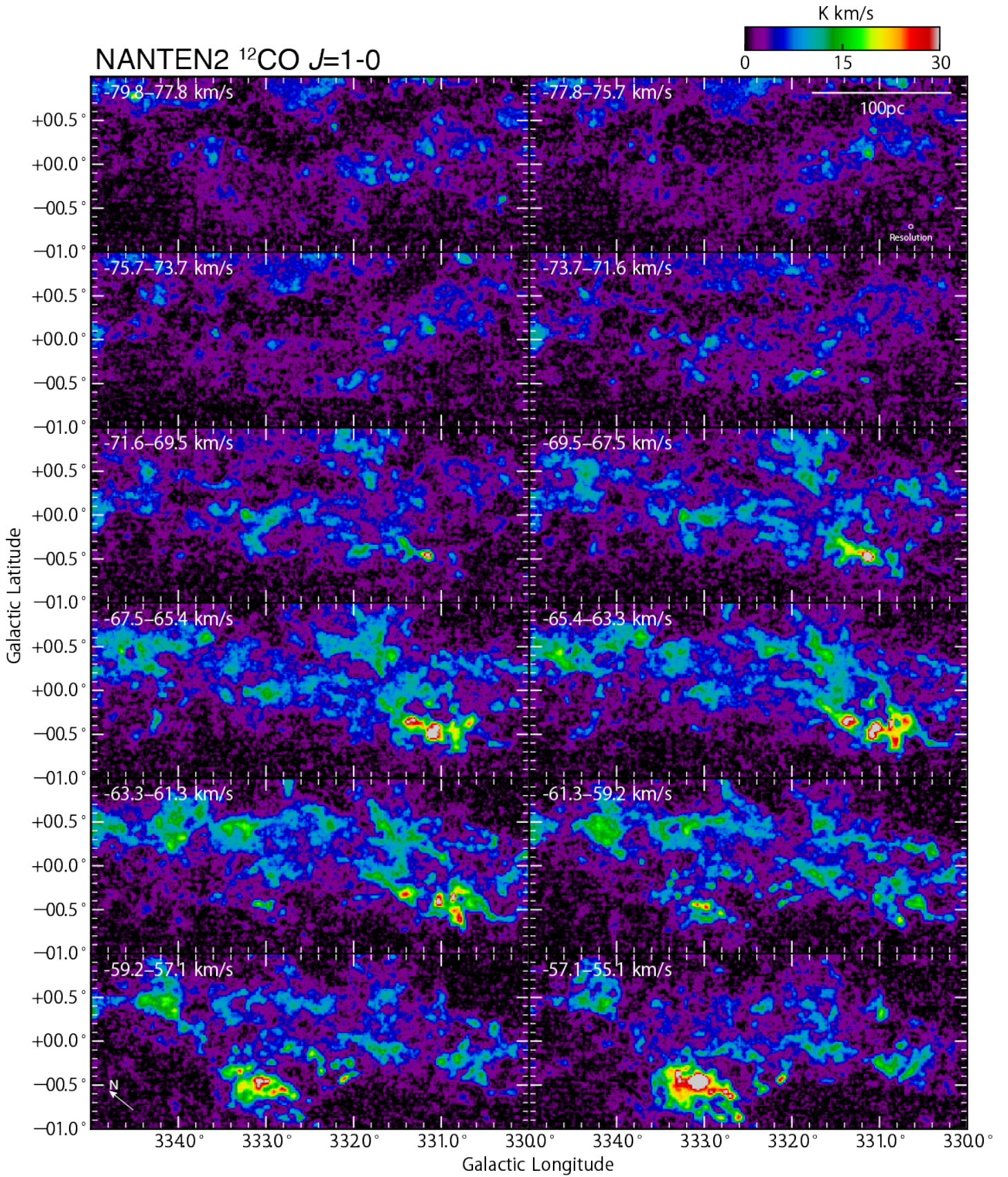


Figure 4. The $^{12}\text{CO } J = 1-0$ velocity channel map obtained by NANTEN2. The cube data is smoothed to the velocity domain of 9 channels by the hanning window. Red dotted rectangles show giant molecular filaments of GMF 335.6–333.6a and GMF 335.6–333.6b.

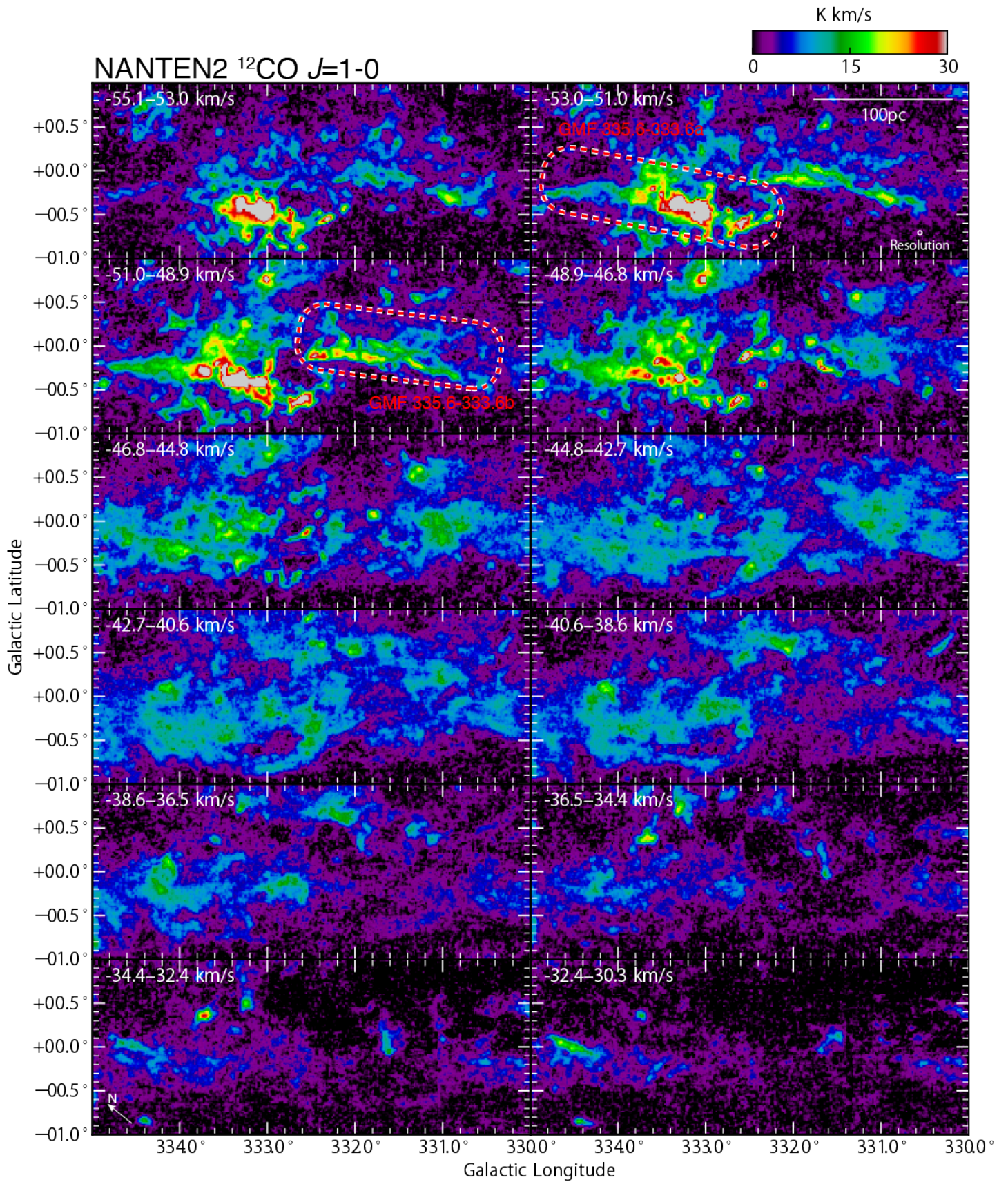


Figure 4. Continued.

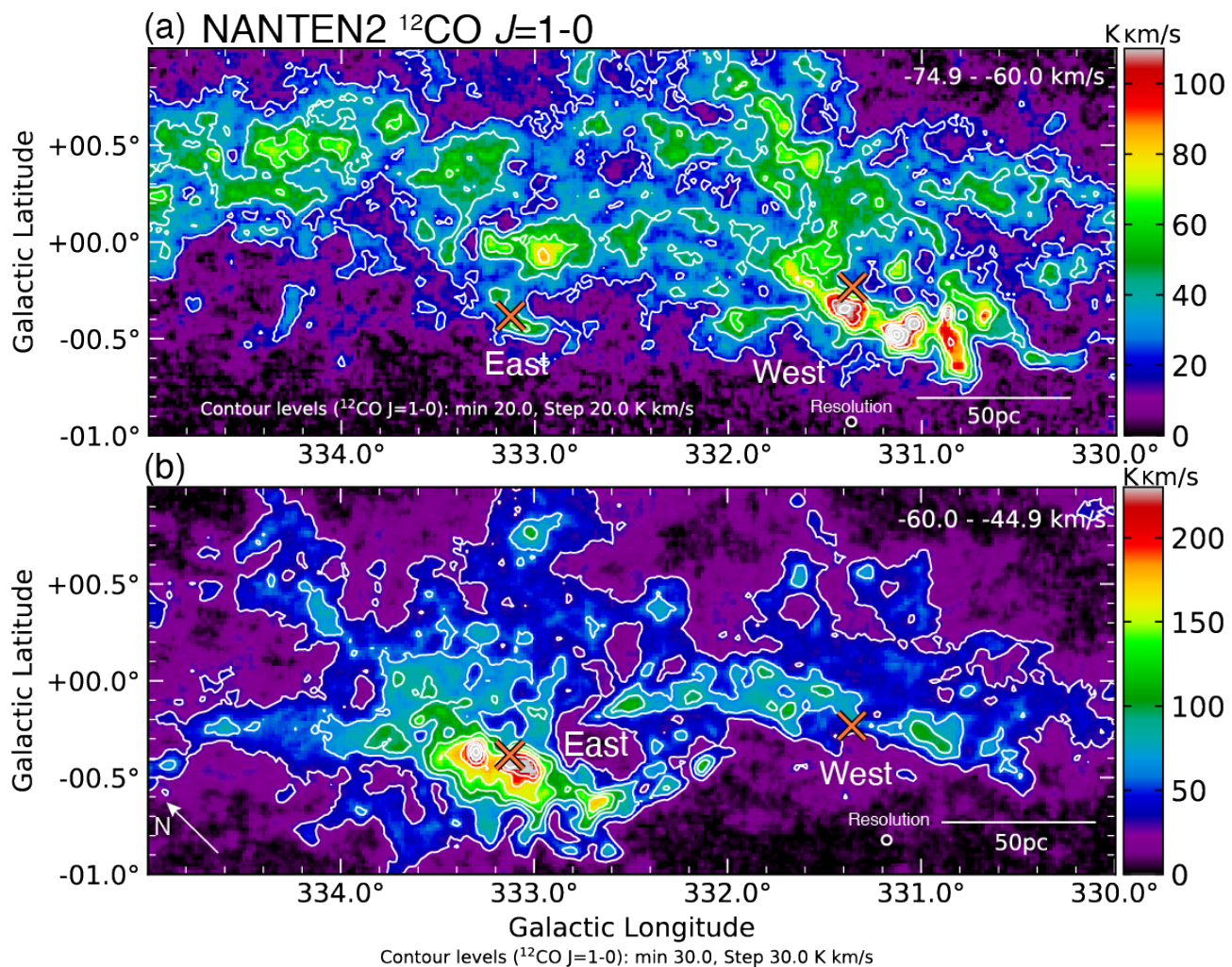


Figure 5. The $^{12}\text{CO } J = 1-0$ integrated intensity maps of (a) the -68 km s^{-1} GMC and (b) -50 km s^{-1} GMC obtained by NANTEN2. The integrated velocity ranges of (a) and (b) are from -75 km s^{-1} to -60 km s^{-1} and from -60 km s^{-1} to -45 km s^{-1} respectively. The lowest contour and interval of the panel (a) are 20 K km s^{-1} and 20 K km s^{-1} , respectively. The lowest contour and interval of the panel (b) are 30 K km s^{-1} and 30 K km s^{-1} , respectively. The orange cross marks at East and West show the position of spectra in Figures 3a and 3b, respectively.

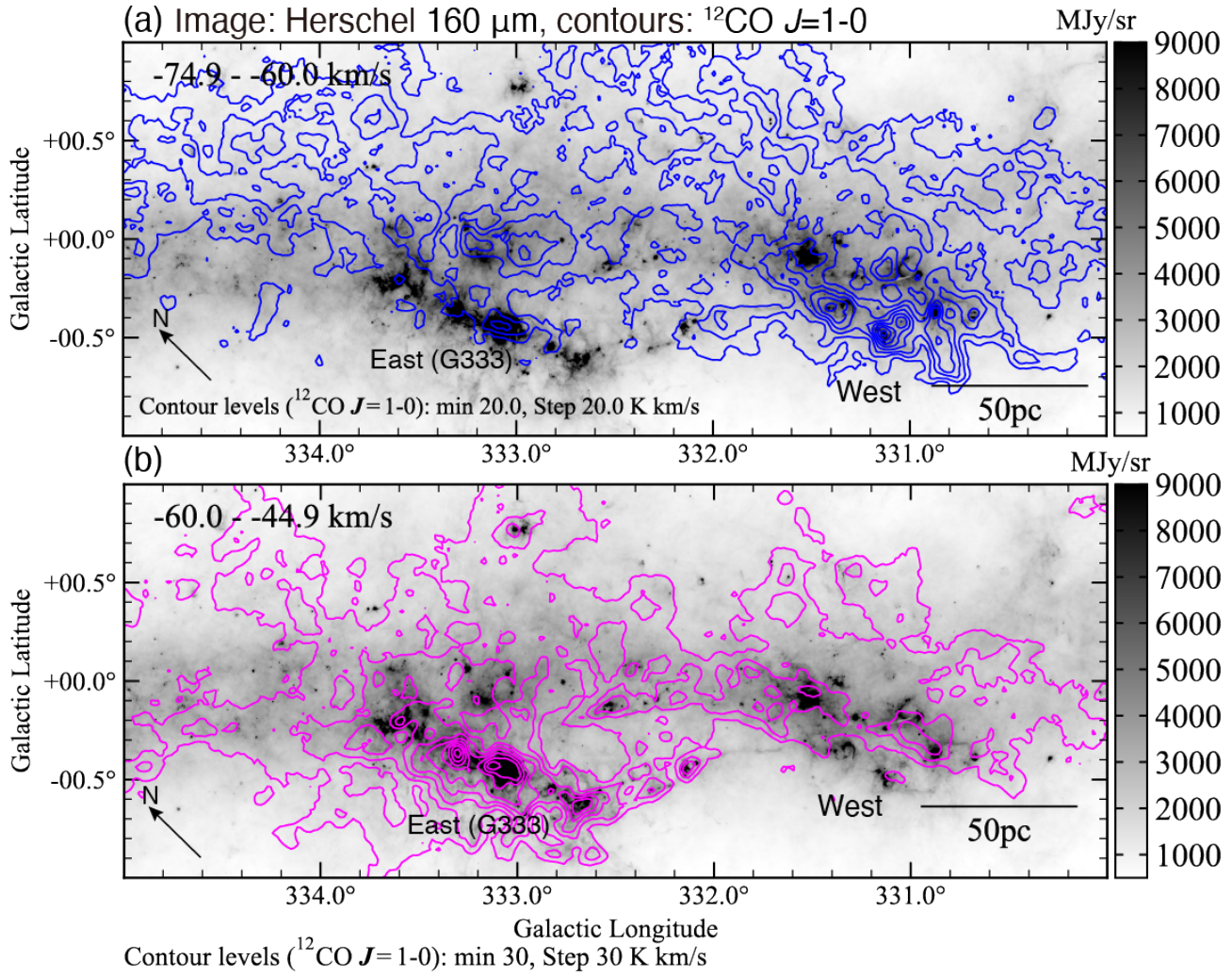


Figure 6. The $^{12}\text{CO } J=1-0$ integrated intensity maps of (a) the -68 km s^{-1} GMC and (b) -50 km s^{-1} GMC obtained by NANTEN2 superposed on the Herschel 160 μm continuum image (Molinari et al. 2010a). The lowest contour and interval of the panel (a) is 20 K km s^{-1} . The lowest contour level and interval of the panel (b) is 30 K km s^{-1} .

3.3. RCW 106 East (G333)

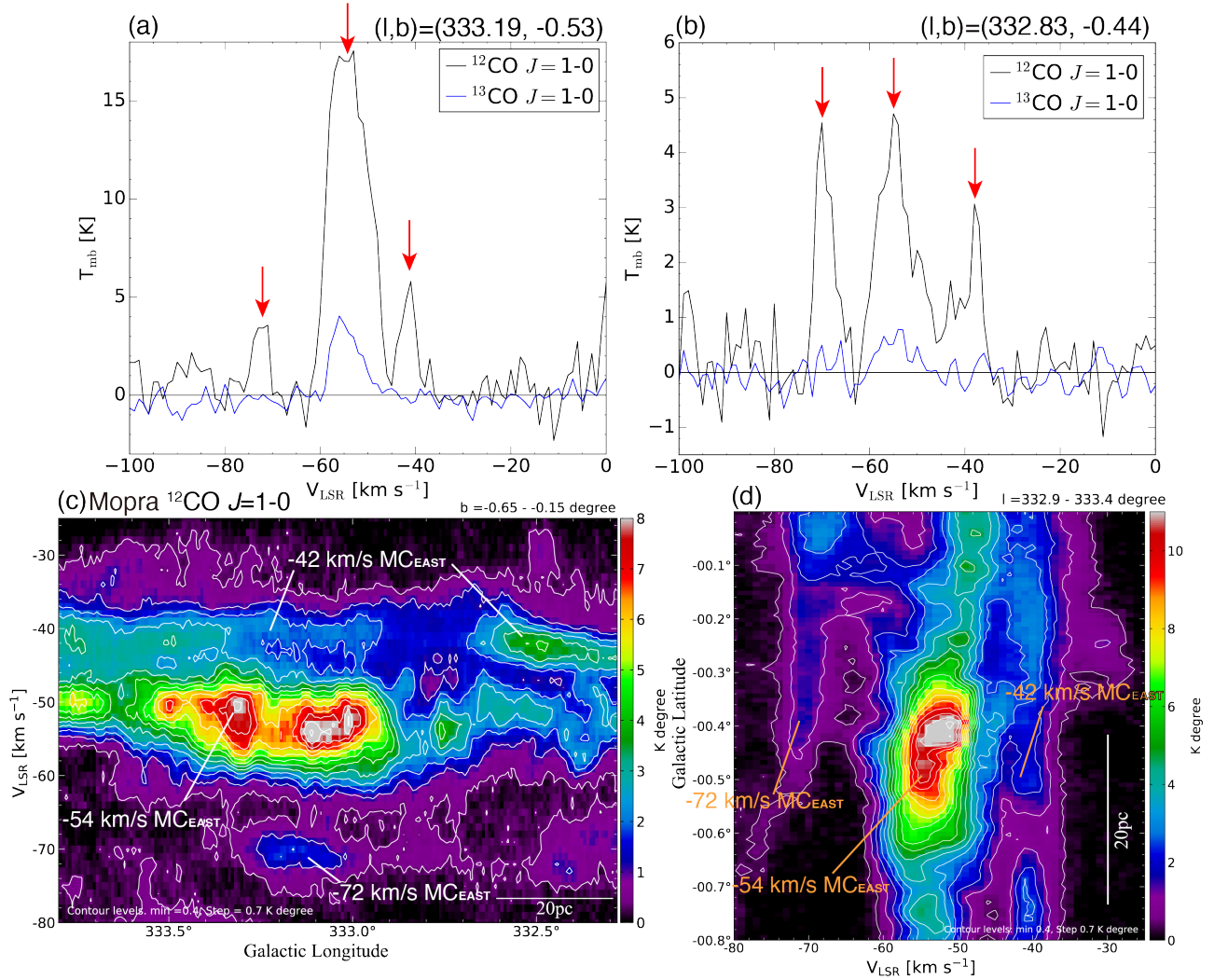


Figure 7. The CO $J = 1-0$ spectra in RCW 106 East at (a) $(l, b) = (333^{\circ}19, -0^{\circ}53)$ and (b) $(l, b) = (332^{\circ}83, -0^{\circ}44)$ obtained by Mopra. Black and blue spectra show ^{12}CO and ^{13}CO $J = 1-0$ emission, respectively. Red arrows present the three velocity components of -72 km s^{-1} , -54 km s^{-1} , and -42 km s^{-1} . The position of spectra in the panel (a) and (b) is the green circles of A and B in Figure 11a, respectively. (c) The ^{12}CO $J = 1-0$ longitude-velocity diagram in RCW 106 East. The integrated latitude range is from $-0^{\circ}65$ to $-0^{\circ}15$. (d) The ^{12}CO $J = 1-0$ latitude-velocity diagram in RCW 106 East. The integrated longitude range is from $332^{\circ}9$ to $333^{\circ}4$. The lowest contour levels and intervals are 0.4 K degree and 0.7 K degree, respectively.

Figures 7(a) and (b) show the CO spectra at $(l, b) = (333^{\circ}19, -0^{\circ}53)$ and $(l, b) = (332^{\circ}83, -0^{\circ}44)$ in RCW 106 East obtained by Mopra, respectively. The positions of the spectra are shown as the green circles of A and B in Figure 11a. We can find that three velocity components of -72 km s^{-1} , -54 km s^{-1} , and -42 km s^{-1} in ^{12}CO $J = 1-0$ shown by red arrows. Hereafter, we call these molecular clouds (MCs) the -72 km s^{-1} MC_{EAST} , -54 km s^{-1} MC_{EAST} , and -42 km s^{-1} MC_{EAST} . Figures 7(c) and (d) present the longitude-velocity and latitude-velocity diagram at RCW 106 East, respectively. These MCs connect on the velocity space in the position-velocity diagrams.

Figures 8(a), (b), and (c) show the -72 km s^{-1} MC_{EAST} , -54 km s^{-1} MC_{EAST} , and -42 km s^{-1} MC_{EAST} superposed on the Herschel $160 \mu\text{m}$ continuum image, respectively. The -72 km s^{-1} MC_{EAST} distributes at the massive star-forming region of G333.6-0.2, IRAS 16177-5018, IRAS 16172-5028, and G333.0-0.4. The -54 km s^{-1} MC_{EAST} is the main intensity component, and molecular gas coincides with infrared peaks. The -42 km s^{-1} MC_{EAST} distributes

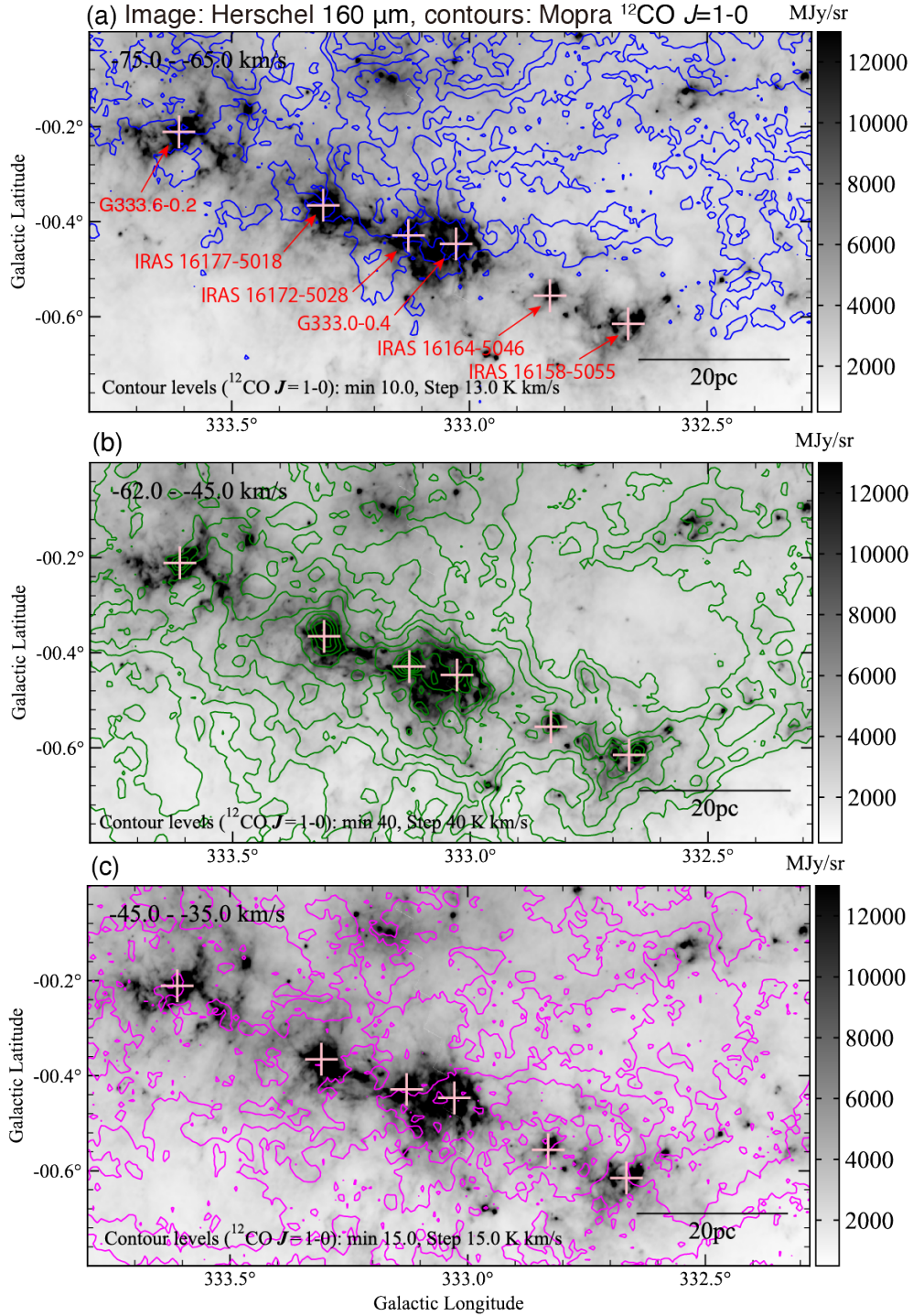


Figure 8. The $^{12}\text{CO } J = 1-0$ integrated intensity maps of the three velocity components in RCW 106 East (G333) superposed on the Herschel $160 \mu\text{m}$ continuum image (Molinari et al. 2010a) for the (a) $-72 \text{ km s}^{-1} \text{ MCEAST}$, (b) $-54 \text{ km s}^{-1} \text{ MCEAST}$, and (c) $-42 \text{ km s}^{-1} \text{ MCEAST}$. The data are smoothed to be $50''$ using a kernel Gaussian function. The cross marks are positions of the massive star-forming regions in RCW 106 East (Bains et al. 2006). The integrated velocity range of $-72 \text{ km s}^{-1} \text{ MCEAST}$, $-54 \text{ km s}^{-1} \text{ MCEAST}$, and $-42 \text{ km s}^{-1} \text{ MCEAST}$ is from -75 km s^{-1} to -65 km s^{-1} , from -62 km s^{-1} to -45 km s^{-1} , and from -45 km s^{-1} to -35 km s^{-1} , respectively. The lowest contour level and interval are 10 K km s^{-1} and 13 K km s^{-1} in the panel (a), 40 K km s^{-1} and 40 K km s^{-1} in the panel (b), 15 K km s^{-1} and 15 K km s^{-1} in the panel (c).

throughout RCW 106 East. We point out that -72 km s^{-1} MC_{EAST} and -54 km s^{-1} MC_{EAST} overlap the massive star-forming regions of G333.6-0.2, IRAS 16172-5028, and G333.0-0.4.

3.4. RCW 106 West

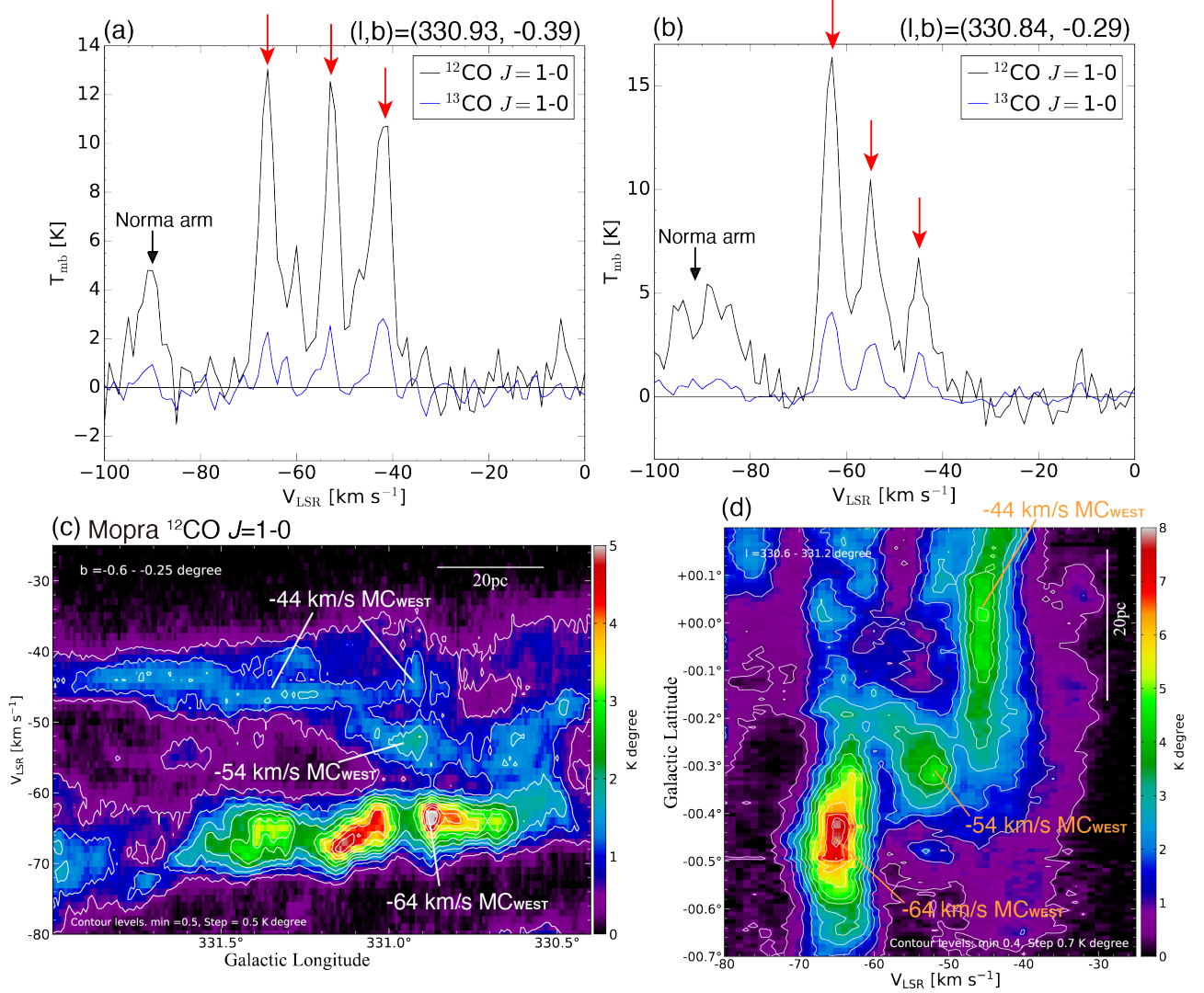


Figure 9. The CO $J = 1-0$ spectra in RCW 106 West at (a) $(l, b) = (330^\circ 93, -0^\circ 39)$ and (b) $(l, b) = (330^\circ 84, -0^\circ 29)$ obtained by Mopra. Black and blue spectra show ^{12}CO and ^{13}CO $J = 1-0$ emission, respectively. Red arrows present the three velocity components of -64 km s^{-1} , -54 km s^{-1} , and -44 km s^{-1} . The black arrows show the velocity components of the Norma arm. The position of spectra in the panel (a) and (b) is the green circles of C and D in Figure 11b, respectively. (c) The ^{12}CO $J = 1-0$ longitude-velocity diagram in RCW 106 West. The integrated latitude range is from $-0^\circ 60$ to $-0^\circ 25$. (d) The ^{12}CO $J = 1-0$ latitude-velocity diagram in RCW 106 West. The integrated longitude range is from $330^\circ 6$ to $331^\circ 2$. The lowest contour levels and intervals are 0.5 K degree in the panel (c). The lowest contour levels and intervals are 0.4 K degree and 0.7 K degree in the panel (d), respectively.

Figures 9(a) and (b) show the CO spectra at $(l, b) = (330^\circ 93, -0^\circ 39)$ and $(l, b) = (330^\circ 84, -0^\circ 29)$ in RCW 106 West. The positions of the spectra are shown as the green circles of C and D in Figure 11b. We can find the three velocity components of -64 km s^{-1} , -54 km s^{-1} , and -44 km s^{-1} in ^{12}CO $J = 1-0$ presented by red arrows. Hereafter, we call these MCs the -64 km s^{-1} MC_{WEST} , -54 km s^{-1} MC_{WEST} , and -44 km s^{-1} MC_{WEST} . The black arrow shows

the Norma arm component. Figures 9(c) and (d) demonstrate the longitude-velocity and latitude-velocity diagrams, respectively. These MCs in RCW 106 West also connect at $l \sim 330^\circ 85$ and $b \sim -0^\circ 30$ on the velocity space.

Figures 10(a),(b), and (c) show the -64 km s^{-1} MC_{WEST}, -54 km s^{-1} MC_{WEST}, and -44 km s^{-1} MC_{WEST} overlaid on the Herschel $160 \mu\text{m}$ continuum image. The main component of -64 km s^{-1} MC_{WEST} has CO peaks corresponding to bright infrared emission at the massive star-forming regions of IRAS 16085–5138, IRAS 16082–5150, and IRAS 16065–5158. In particular, -64 km s^{-1} MC_{WEST} and -54 km s^{-1} MC_{WEST} are overlapped at IRAS 16065–5158 and coincide molecular gas with the infrared peak.

We estimated the physical parameters of the MCs in RCW 106 East and RCW 106 West with data points above the 5σ noise levels in ^{12}CO and ^{13}CO $J = 1-0$. The parameters are excitation temperature (T_{ex}), optical depth (τ_{13}), H_2 column density, and total molecular mass calculated from the ^{12}CO and ^{13}CO $J = 1-0$ intensity. Detailed procedures are presented in Appendix A. We summarize the results in Table 2.

3.5. Physical association of two MCs in RCW 106 East and West

The -42 km s^{-1} MC_{EAST} and -44 km s^{-1} MC_{WEST} spatially extended distributions and no clumpy structures (see Figures 4, 8c, and 10c). Russeil et al. (2005) shows that these velocity components are associated with the young supernova remnant RCW 103 and Wolf-Rayet nebula RCW 104 as more evolved regions of RCW 106 from a velocity-resolved deep $\text{H}\alpha$ survey. We point out that -42 km s^{-1} MC_{EAST} and -44 km s^{-1} MC_{WEST} might be diffuse foreground components at the front face of the Scutum-Centarus arm. To summarize our result, focusing on the RCW 106 East and West regions internal the RCW 106 GMC complex, these regions comprise two MCs with $\sim 10 \text{ km s}^{-1}$ differences associated with massive star-forming regions.

Table 2. Physical properties of molecular clouds in RCW 106 East and West.

Name	T_{ex}	τ_{13}	$N_{\text{X}}^{12} \text{ max}$	$N_{\text{X}}^{12} \text{ mean}$	$N_{\text{LTE}}^{13} \text{ max}$	$N_{\text{LTE}}^{13} \text{ mean}$	M_{X}^{12}	M_{LTE}^{13}
(1)	[K]	(3)	[cm^{-2}]	[cm^{-2}]	[cm^{-2}]	[cm^{-2}]	[M_{\odot}]	[M_{\odot}]
(1)	(2)	(3)	(4)	(5)	(6)	(7)	(8)	(9)
RCW 106 East (total)	16	0.30	1.1×10^{23}	2.1×10^{22}	2.8×10^{23}	1.5×10^{22}	2.2×10^6	1.2×10^6
-72 km s^{-1} MC _{EAST}	15	0.33	1.4×10^{22}	8.0×10^{20}	1.1×10^{22}	2.4×10^{21}	8.6×10^4	1.1×10^4
-54 km s^{-1} MC _{EAST}	16	0.30	9.5×10^{22}	1.5×10^{22}	2.7×10^{23}	1.5×10^{22}	1.6×10^6	9.9×10^5
-42 km s^{-1} MC _{EAST}	18	0.38	1.6×10^{22}	5.2×10^{21}	2.7×10^{22}	2.6×10^{21}	5.6×10^5	1.1×10^5
RCW 106 West (total)	12	0.32	6.6×10^{22}	1.2×10^{22}	9.7×10^{22}	5.9×10^{21}	1.6×10^6	4.6×10^5
-64 km s^{-1} MC _{WEST}	12	0.29	4.1×10^{22}	5.5×10^{21}	8.4×10^{22}	6.5×10^{21}	7.0×10^5	2.5×10^5
-54 km s^{-1} MC _{WEST}	11	0.31	2.3×10^{22}	3.2×10^{21}	2.5×10^{22}	3.4×10^{21}	4.1×10^5	9.1×10^4
-44 km s^{-1} MC _{WEST}	10	0.35	1.6×10^{22}	3.7×10^{21}	2.1×10^{22}	2.4×10^{21}	4.7×10^5	1.1×10^5

Notes. — Columns: (1) The cloud name. (2) The mean excitation temperature obtained by the ^{12}CO peak intensity. (3) The mean optical depth obtained by ^{13}CO . (4) The peak H_2 column density derived from ^{12}CO assuming the X_{CO} factor. (5) The mean H_2 column density calculated from ^{12}CO assuming the X_{CO} factor. (6) The peak H_2 column density derived from ^{13}CO assuming LTE. (7) The mean H_2 column density derived from ^{13}CO assuming LTE. (8) The total molecular mass estimated from the H_2 column density assuming the X_{CO} factor. (9) The total molecular mass estimated from the H_2 column density assuming LTE. The physical properties are derived above the 5σ noise level in the ^{12}CO and ^{13}CO cube data.

4. DISCUSSION

4.1. The scenario of massive stars/cluster formation in the RCW 106 GMC complex

Our detailed analysis of RCW 106 East and RCW 106 West indicates that the two MCs having a velocity difference of $\sim 10 \text{ km s}^{-1}$ are physically associated with massive star-forming regions in the RCW 106 GMC complex. Figures 11(a) and 11(b) show the overlaid spatial distributions of two MCs focusing on RCW 106 East and RCW 106 West, respectively. These MCs overlap around massive star-forming regions of G333.6-0.2, IRAS 16172-5028, G333.0-0.4 in RCW 106 East, and IRAS 16065-5158 in RCW 106 West. This observational feature is consistent with the signature of cloud-cloud collisions reported by previous studies of Galactic min-starburst region NGC 6334 (see Figure 8 in Fukui

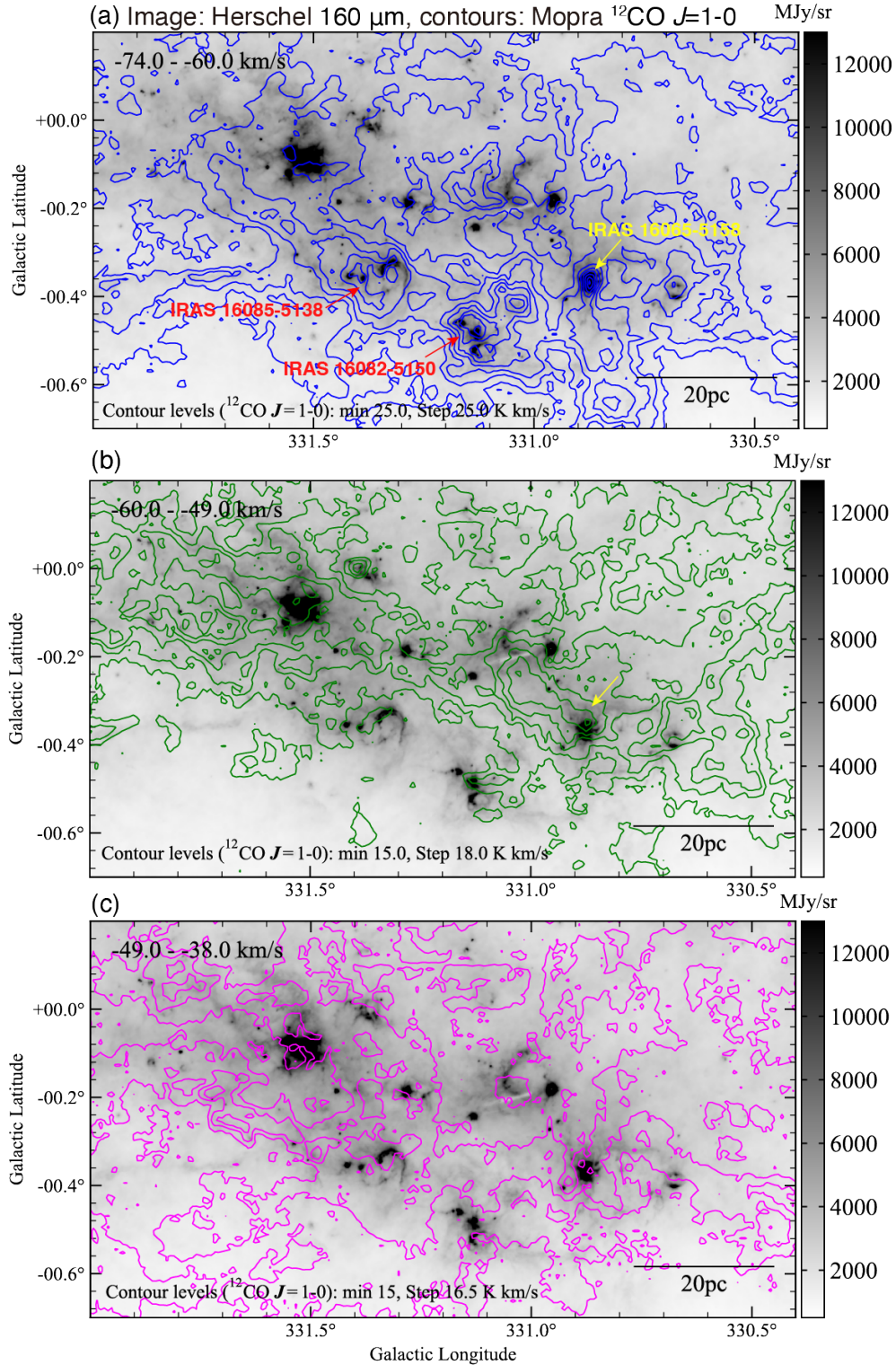


Figure 10. The $^{12}\text{CO } J = 1-0$ integrated intensity maps of the three velocity components in RCW 106 West superposed on the Herschel 160 μm continuum image (Molinari et al. 2010a) for the (a) -64 km s^{-1} MC_{WEST}, (b) -54 km s^{-1} MC_{WEST}, and (c) -44 km s^{-1} MC_{WEST}. The data are smoothed to be $50''$ using a kernel Gaussian function. The integrated velocity range of -64 km s^{-1} MC_{WEST}, -54 km s^{-1} MC_{WEST}, and -44 km s^{-1} MC_{WEST} is from -74 km s^{-1} to -60 km s^{-1} , from -60 km s^{-1} to -49 km s^{-1} , and from -49 km s^{-1} to -38 km s^{-1} , respectively. The lowest contour level and interval are 25 K km s^{-1} and 25 K km s^{-1} in the panel (a), 15 K km s^{-1} and 18 K km s^{-1} in the panel (b), 15 K km s^{-1} and 16.5 K km s^{-1} in the panel (c).

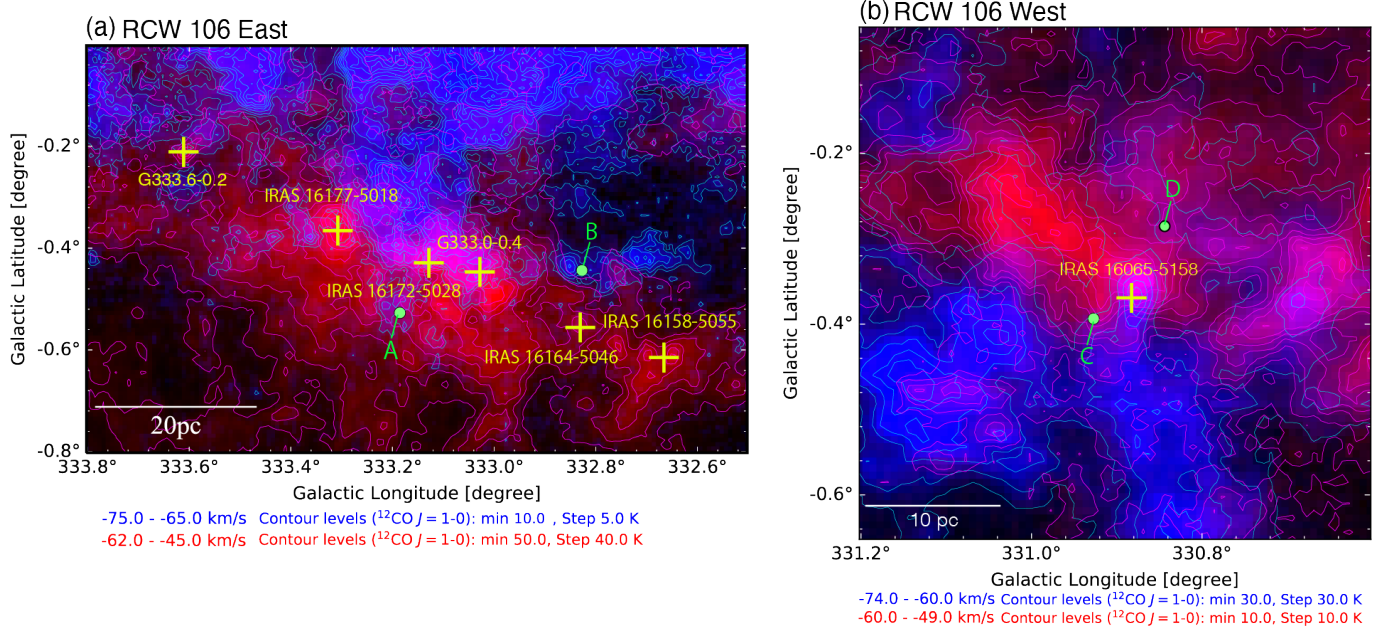


Figure 11. The two-color composite image of the $^{12}\text{CO } J=1-0$ integrated intensity distributions obtained by Mopra. (a) The blue and red image represent $-72 \text{ km s}^{-1} \text{ MC}_{\text{EAST}}$ and $-54 \text{ km s}^{-1} \text{ MC}_{\text{EAST}}$, respectively. The integrated velocity ranges and yellow crosses are the same as Figure 8. The lowest contour levels and intervals are 10 K km s^{-1} and 5 K km s^{-1} in $-72 \text{ km s}^{-1} \text{ MC}_{\text{EAST}}$, 50 K km s^{-1} and 40 K km s^{-1} in $-54 \text{ km s}^{-1} \text{ MC}_{\text{EAST}}$, respectively. (b) The blue and red image represent $-64 \text{ km s}^{-1} \text{ MC}_{\text{WEST}}$ and $-54 \text{ km s}^{-1} \text{ MC}_{\text{WEST}}$ obtained by Mopra, respectively. The integrated velocity ranges and yellow cross are the same as Figure 10. The lowest contour levels and intervals are 30 K km s^{-1} and 30 K km s^{-1} in $-64 \text{ km s}^{-1} \text{ MC}_{\text{WEST}}$, 10 K km s^{-1} and 10 K km s^{-1} in $-54 \text{ km s}^{-1} \text{ MC}_{\text{WEST}}$, respectively. The green circles of A, B, C, and D show the position of spectra in Figure 7a, Figure 7b, Figure 9a, and Figure 9b, respectively.

et al. 2018b). Figure 12 (a) and (b) show the position-velocity diagrams focusing on the massive star-forming regions in RCW 106 East and West, respectively. We can find the bridge features connecting two CO velocity components on the velocity space. If two molecular clouds collide and interact, we can observe the bridging feature connecting in the velocity space on the position-velocity diagram by comparing CO observations with synthetic observations (Haworth et al. 2015a,b; Torii et al. 2017; Bisbas et al. 2017). We suggest that these results indicate the signature of the interaction between two molecular clouds in RCW 106 East and West. We comment on the viewing angle effects and expected velocity of the star-forming regions formed by colliding two clouds. Fukui et al. (2018a) argued the projection and viewing angle effects distort the contact interface layer on the position-velocity diagram comparing cloud-cloud collision in the Orion nebula cluster with the simulation model by Takahira et al. (2014) and Haworth et al. (2015a,b). In RCW106 East, the Hugal compact sources have velocities around -53 km s^{-1} , and in RCW106 West, they have velocities around -65 km s^{-1} (Mège et al. 2021). In the cloud-cloud collision model with internal turbulent motion, different sizes, and densities, the shock-compressed layer formed by momentum exchange does not necessarily have to be an intermediate velocity of the two colliding clouds (e.g., Takahira et al. 2014; Haworth et al. 2015b). In addition, the velocities of massive clumps formed by cloud-cloud collision can have offsets from the intermediate velocity of two colliding clouds because shock compression enhances turbulence in the compressed layer (Inoue & Fukui 2013; Fukui et al. 2021b).

Figure 13 shows the schematic picture of our proposed scenario. Figure 13(a) illustrates the location of the RCW 106 GMC complex in the Scutum-Centaurus arm of the Milky Way. Molecular clouds, whose sizes and masses of $\sim 20\text{--}30 \text{ pc}$ and $\sim 10^4\text{--}10^6 M_{\odot}$ collide with the supersonic velocity of $\sim 10 \text{ km s}^{-1}$, as shown in Figure 13(b). The shock compression by supersonic collisions of molecular clouds produces dense cores and triggers massive star/cluster formation (see the review paper of Fukui et al. 2021a). Indeed, the numerical simulations show that supersonic cloud-cloud collisions having different sizes and densities can produce massive molecular cloud cores required for massive star formation at the interface layer by shock compression (Habe & Ohta 1992; Anathpindika 2010; Takahira et al. 2014, 2018; Shima et al. 2018). Recent simulations considering magnetic fields also reveal massive dense cores produced by

cloud-cloud collisions (Inoue & Fukui 2013; Wu et al. 2015; Fukui et al. 2021b; Sakre et al. 2021; Kinoshita & Nakamura 2022; Kashiwagi et al. 2023). Kobayashi et al. (2018) point out that most cloud collision events occur between GMCs

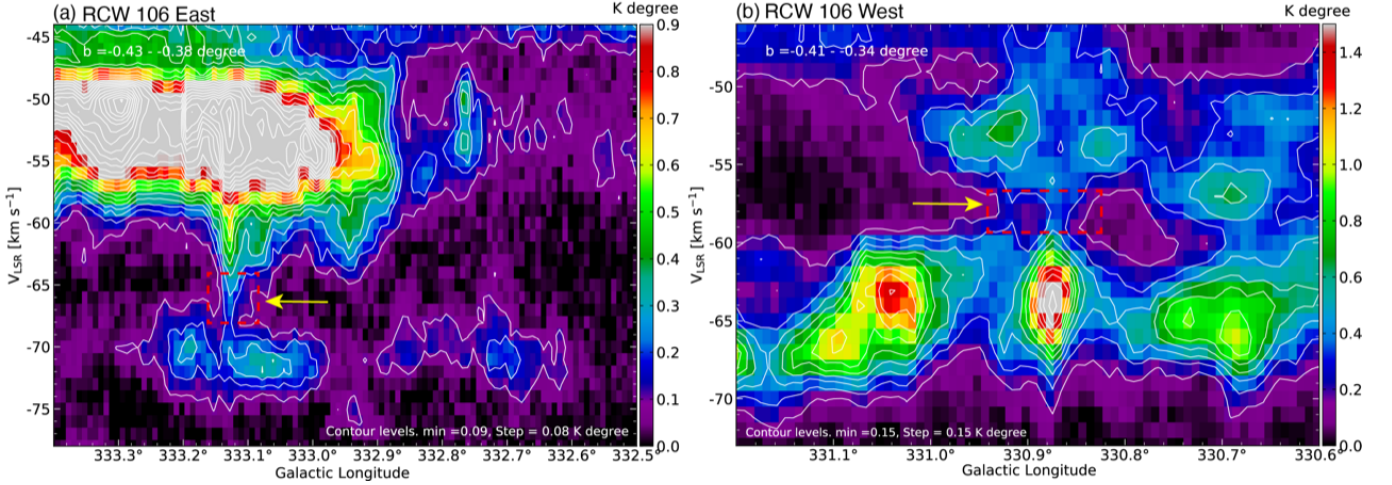


Figure 12. Detailed $^{12}\text{CO } J=1-0$ longitude-velocity diagrams of (a) RCW 106 East and (b) RCW 106 West. The integrated latitude ranges of (a) and (b) are from -0.43° to -0.38° and from -0.41° to -0.34° , respectively. The lowest contour levels of (a) and (b) are 0.09 K degree and 0.15 K degree. The contour intervals of (a) and (b) are 0.08 K degree and 0.15 K degree. The red-dotted rectangles and yellow arrows show the bridge features connecting two velocity components.

with the mass of $\lesssim 10^{5.5} M_\odot$ from their calculation for the time evolution of the GMC mass function. The numerical simulation by Horie et al. (2024) suggested that collisions of molecular clouds with masses of $\sim 10^4-10^5 M_\odot$ at relative velocities of $\sim 10-20 \text{ km s}^{-1}$ could occur in the spiral arm of the Milky Way-like galaxy. These theoretical studies support our proposed scenario and observational signatures of the RCW 106 GMC complex.

4.2. Cloud-cloud collisions in the RCW 106 GMC complex

In this section, we describe our cloud-cloud collision model in this region as the interpretation of observational results. The RCW 106 GMC complex has the orientation of star formation slightly inclined to the galactic plane (see Figure 1a). This might be explained by cloud collisions having the inclined momentum to the Galactic plane. Our results of the morphology of the GMCs and their large projected distance could be explained by the Galactic scale dynamics such as spiral shocks or shear motions (e.g., Dobbs & Baba 2014; Tokuda et al. 2020; Kohno et al. 2022). Indeed, the Galactic-scale simulation of the cloud-cloud collision shows that the GMCs have elongated and filamentary structures due to Galactic dynamics (see Figure 14 in Horie et al. 2024). These GMCs expect to experience the collision event in their lifetime. RCW 106 East has more molecular mass than RCW 106 West, and the current evolved star formation indicate to be driven by the collision of more massive molecular clouds. RCW 106 West is still in the early stages of cloud collision and might develop into an extremely star formation in the future. In Figures 4, 8, and 10, we can find that $-72 \text{ km s}^{-1} \text{ MC}_{\text{EAST}}$ and $-54 \text{ km s}^{-1} \text{ MC}_{\text{WEST}}$ appear spatially small distributions. The observed these clumpy structures in RCW 106 East and West might be affected by two processes both molecular clouds are originally clumpy and cloud-cloud collisions form dense clumps. The three-dimensional magnetohydrodynamic simulation shows that the colliding HI gas flow forms molecular clouds, and clumpy structures are created in the diffuse molecular gas (Inoue & Inutsuka 2012; Kobayashi et al. 2023). The cloud-cloud collision scenario also forms dense clumps at the collision interface due to shock compression (e.g., Takahira et al. 2014, 2018; Inoue et al. 2018).

4.3. Comparison with properties of Galactic mini-starburst regions associated with the GMC complex.

Finally, we compared the physical properties of molecular clouds associated with the Galactic mini-starbursts triggered by the cloud-cloud collision in the Milky Way. Table 3 summarizes the properties of GMC complexes on the spiral arm in the Milky Way. Enokiya et al. (2021) conducted statistical studies on massive star-forming regions that reported cloud-cloud collisions. The authors suggest that the condition of > 10 O-type star formation is the peak column density of $N(\text{H}_2) > 10^{23} \text{ cm}^{-2}$. Recent magnetohydrodynamic simulations of shock compression caused by

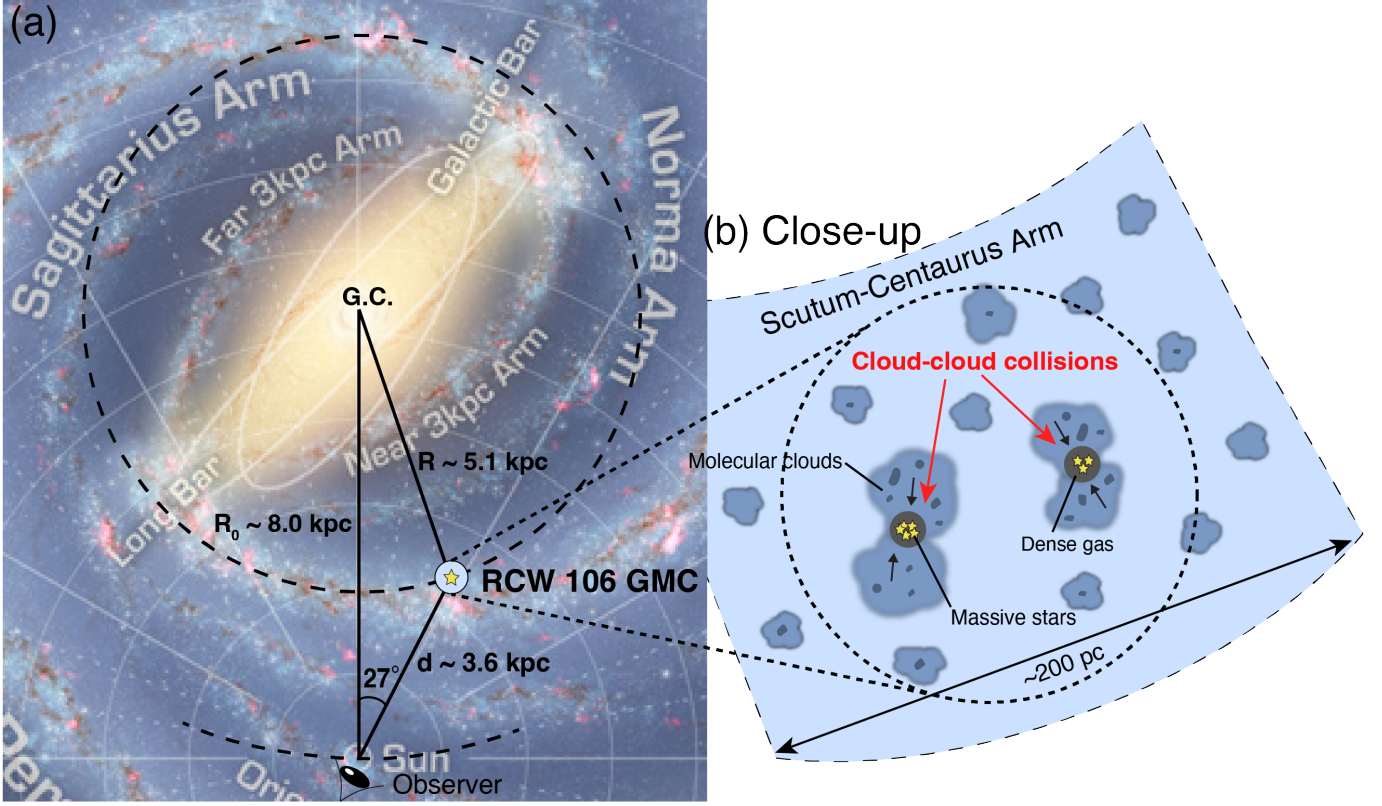


Figure 13. (a) The location at the RCW 106 GMC complex superposed on the face-on illustration of the Milky Way (NASA/JPL-Caltech/ESO/R. Hurt). The distance to the Galactic center (R_0) is adapted from the Very Long Baseline Interferometry (VLBI) astrometry results (Reid et al. 2019; VERA Collaboration et al. 2020). (b) Schematic illustration of our proposed massive star/cluster formation scenario in the RCW 106 GMC complex.

Table 3. Comparison with the Galactic mini-starbursts induced by cloud-cloud collisions in the GMC complex.

Name	l [degree]	b [degree]	Distance [kpc]	Luminosity [L_\odot]	Relative velocity [km s^{-1}]	$N(\text{H}_2)_{\text{max}}$ [cm^{-2}]	Molecular mass [M_\odot]	References
(1)	(2)	(3)	(4)	(5)	(6)	(7)	(8)	(9)
RCW 106 East	333.60	-0.20	3.6	4.8×10^6	~ 10	$\sim 3 \times 10^{23}$	$\sim 2 \times 10^6$	This work
W33	12.80	-0.20	2.4	1.2×10^6	~ 23	$\sim 6 \times 10^{23}$	$\sim 9 \times 10^5$	[1,2,3,4]
W43 Main	30.80	-0.05	5.5	5.2×10^6	$\sim 10\text{-}30$	$\sim 3 \times 10^{23}$	$\sim 2 \times 10^6$	[5,6,7]
W49A	43.16	0.00	11.11	1.6×10^7	~ 8	$\sim 8 \times 10^{23}$	$\sim 1 \times 10^6$	[8,9]
W51A	49.5	-0.04	5.4	1.8×10^7	$\sim 4\text{-}20$	$\sim 3 \times 10^{23}$	$\sim 6 \times 10^5$	[10,11]
NGC 6334	351.20	0.70	1.7	2.7×10^6	~ 12	$\sim 8 \times 10^{22}$	$\sim 2 \times 10^5$	[12,13]
NGC 6357	353.20	0.80	1.7	4.3×10^6	~ 12	$\sim 4 \times 10^{22}$	$\sim 2 \times 10^5$	[12,14]
Carina	287.40	-0.6	2.3	1.8×10^7	$\sim 6\text{-}20$	$\sim 5 \times 10^{22}$	$\sim 8 \times 10^4$	[15,16,17]

Notes. — Col. (1) Region name. Col. (2) Galactic longitude. Col. (3) Galactic latitude. Col. (4) Distance from the solar system. Col. (5) Total infrared luminosity obtained by Binder & Povich (2018). Col. (6) The radial velocity difference between colliding molecular clouds. Col. (7) The peak H_2 column density. (8) Total molecular mass. (9) References. [1] Kohno et al. (2018) [2] Dewangan et al. (2020) [3] Murase et al. (2022) [4] Zhou et al. (2023) [5] Kohno et al. (2021) [6] Sofue et al. (2019) [7] Motte et al. (2003) [8] Miyawaki et al. (2022) [9] Galván-Madrid et al. (2013) [10] Fujita et al. (2021a) [11] Okumura et al. (2001) [12] Fukui et al. (2018b) [13] Arzoumanian et al. (2022) [14] Russeil et al. (2019) [15] Fujita et al. (2021b) [16] Yonekura et al. (2005) [17] Rebolledo et al. (2016)

colliding flows support this initial condition as a massive cluster formation (Abe et al. 2022). We point out that RCW 106 East has a peak column density of $3 \times 10^{23} \text{ cm}^{-2}$ and satisfies this condition. The relative velocity of $\sim 10\text{--}20 \text{ km s}^{-1}$ are common to the mini-starburst regions produced by cloud-cloud collisions. Thus, we propose that the supersonic cloud collision events of $\sim 10\text{--}20 \text{ km s}^{-1}$ are essential to achieve extreme star/cluster formation in the Milky Way.

The total molecular mass of RCW 106 East is $2 \times 10^6 M_{\odot}$. It is massive compared with other GMCs on the spiral arm in Table 3. Therefore, RCW 106 East is an agglomerate of molecular gas in the Scutum-Centaurus arm and cloud-cloud collisions in this region are likely to be more frequent than the galactic disk's average. The collision rate of spherical molecular clouds on the galactic disk is estimated as

$$t_{\text{coll}} = \frac{\lambda}{v_c} = \frac{1}{\pi r^2 n v_c}, \quad (1)$$

where λ is the mean free path, r is the radius of molecular clouds, n is the number density of molecular clouds, and v_c is the relative velocity of a cloud-cloud collision, respectively. The number of clouds in the RCW 106 GMC complex is simply estimated to be $9.5 \times 10^6 / 7.0 \times 10^5 \sim 13.6$ from the ratio of the ^{12}CO total molecular mass in the GMC complex and mean molecular mass of the colliding clouds. The number density is derived to be $n \sim 4.2 \times 10^{-6} \text{ pc}^{-3}$ from the number of clouds if we assume a volume space of $200 \text{ pc} \times 200 \text{ pc} \times 80 \text{ pc}$. The collision velocity is adopted as $v_c = 10 \times \sqrt{3} \sim 17 \text{ km s}^{-1}$ assuming a viewing angle of 45° along the collision axis in the three-dimensional space. Taking a radius of molecular clouds of 20 pc , we obtain $t_{\text{coll}} \sim 11 \text{ Myr}$. The total lifetime of GMCs is typically $\sim 10\text{--}30 \text{ Myr}$ obtained by the statistical studies of GMCs in nearby galaxies (Kawamura et al. 2009; Chevance et al. 2023; Konishi et al. 2024; Demachi et al. 2024). The collision rate of the RCW 106 GMC complex is $\sim 11 \text{ Myr}$, which is comparable to the typical lifetime of GMCs. We point out that this result is likely to experience cloud collisional events more than once in its lifetime at this position in the Galaxy. Indeed, numerical simulations also suggest that a massive GMC experiences several collisional events in its lifetime (Tasker & Tan 2009; Tasker 2011; Fujimoto et al. 2014; Dobbs et al. 2015; Kobayashi et al. 2017, 2018). We suggest that cloud-cloud collisions predicted by these Galactic-scale simulations occur in RCW 106 GMC complex on the Scutum-Centaurus arm, and triggering extreme star formation events known as mini-starbursts.

5. CONCLUSION

The summary of this paper is as follows:

1. We observed the southern massive star-forming region of RCW 106 (G333) GMC complex using a NANTEN2 4-m radio telescope in Chile operated by Nagoya University. We also analyzed the Mopra CO Galactic plane survey and Herschel dust continuum data, which revealed the origin of the mini-starburst in the RCW 106 GMC complex.
2. The RCW 106 GMC complex comprises two radial velocity components of -68 km s^{-1} and -50 km s^{-1} (Nguyen et al. 2015). Using the Mopra CO data, our detailed analysis revealed three velocity components at the RCW 106 East and RCW 106 West, with the bright infrared dust emission involved in massive star/cluster formation.
3. The two out of three velocity components in RCW 106 East and RCW 106 West coincide CO peaks with infrared dust emission and connect each other with the bridge feature on the position-velocity diagram. Thus, these two velocity components having a velocity difference of $\sim 10 \text{ km s}^{-1}$ are likely to be physically associated with massive star-forming regions and interact with each other in the RCW 106 GMC complex. We suggest that massive star/cluster formation in the RCW 106 GMC complex might be induced by supersonic cloud collisions in the Scutum-Centaurus arm.
4. The RCW 106 East has the peak H_2 column density of $N(\text{H}_2) > 10^{23} \text{ cm}^{-2}$. This column density is satisfied with the initial condition of > 10 O-type star formation reported by previous studies of other massive star-forming regions (Enokiya et al. 2021). The total mass of RCW 106 East is $\sim 2 \times 10^6 M_{\odot}$, which is massive compared with other mini-starburst regions in the Milky Way. We point out that cloud-cloud collisions frequently occur in the RCW 106 GMC complex on the Scutum-Centaurus arm, which might trigger extreme star/cluster formation.

We are grateful to the anonymous referee for carefully reading our manuscript and giving us thoughtful suggestions, which greatly improved this paper.

The NANTEN project is based on a mutual agreement between Nagoya University and the Carnegie Institution of Washington (CIW). We greatly appreciate the hospitality of all the staff members of the Las Campanas Observatory of CIW. We are thankful to many Japanese public donors and companies who contributed to the realization of the project.

NANTEN2 is an international collaboration of eleven universities: Nagoya University, Gifu University, Osaka Metropolitan University, University of Cologne, University of Bonn, Seoul National University, University of Chile, University of New South Wales, Macquarie University, University of Sydney, and Zurich Technical University.

The authors are grateful to Dr. Michael Burton of the University of New South Wales and the Armagh Observatory and Planetarium for the archival CO survey data with Mopra. We also thank Dr. Graeme Wong for kindly supporting remote observations from Nagoya University.

The Mopra radio telescope is part of the Australia Telescope National Facility, which is funded by the Australian Government for operation as a National Facility managed by CSIRO. The University of New South Wales Digital Filter Bank used for the observations with the Mopra Telescope was provided with support from the Australian Research Council.

The Herschel spacecraft was designed, built, tested, and launched under a contract to ESA managed by the Herschel/Planck Project team by an industrial consortium under the overall responsibility of the prime contractor Thales Alenia Space (Cannes), and including Astrium (Friedrichshafen) responsible for the payload module and for system testing at spacecraft level, Thales Alenia Space (Turin) responsible for the service module, and Astrium (Toulouse) responsible for the telescope, with in excess of a hundred subcontractors.

PACS has been developed by a consortium of institutes led by MPE (Germany) and including UVIE (Austria); KU Leuven, CSL, IMEC (Belgium); CEA, LAM (France); MPIA (Germany); INAF-IFSI/OAA/OAP/OAT, LENS, SISSA (Italy); IAC (Spain). This development has been supported by the funding agencies BMVIT (Austria), ESA-PRODEX (Belgium), CEA/CNES (France), DLR (Germany), ASI/INAF (Italy), and CICYT/MCYT (Spain).

SPIRE has been developed by a consortium of institutes led by Cardiff University (UK) and including Univ. Lethbridge (Canada); NAOC (China); CEA, LAM (France); IFSI, Univ. Padua (Italy); IAC (Spain); Stockholm Observatory (Sweden); Imperial College London, RAL, UCL-MSSL, UKATC, Univ. Sussex (UK); and Caltech, JPL, NHSC, Univ. Colorado (USA). This development has been supported by national funding agencies: CSA (Canada); NAOC (China); CEA, CNES, CNRS (France); ASI (Italy); MCINN (Spain); SNSB (Sweden); STFC, UKSA (UK); and NASA (USA).

Facilities: NANTEN: 4 m, NANTEN2: 4 m, Mopra: 22 m, Herschel

Software: Astropy (Astropy Collaboration et al. 2013, 2018, 2022), NumPy (van der Walt et al. 2011), Matplotlib (Hunter 2007), IPython (Perez, & Granger 2007), Miriad (Sault et al. 1995), and APLpy (Robitaille & Bressert 2012)

APPENDIX

A. PROCEDURES DERIVING THE PHYSICAL PROPERTIES OF MOLECULAR CLOUDS

We calculated the physical properties of molecular clouds from the ^{12}CO and ^{13}CO line intensity, assuming the CO-to- H_2 conversion factor (X_{CO}) and Local Thermodynamic Equilibrium (LTE). We present their detailed methods in this appendix.

A.1. The $X(\text{CO})$ method

The H_2 column density using $X(\text{CO})$ is given by

$$N(\text{H}_2)_{12x} = X_{\text{CO}} I_{12\text{CO}} [\text{cm}^{-2}], \quad (\text{A1})$$

where $I_{12\text{CO}}$ is the integrated intensity of ^{12}CO $J = 1-0$. In this paper, we used $X_{\text{CO}} = 2 \times 10^{20} [\text{cm}^{-2} (\text{K km s}^{-1})^{-1}]$ as the standard value of the Galactic disk in the Milky Way (Bolatto et al. 2013).

A.2. The LTE method

We derived the excitation temperature (T_{ex}), optical depth (τ_{13}), and column density of molecular clouds ($N_{13\text{CO}}$) assuming the LTE as described in Pineda et al. (2008); Sofue & Kohno (2020), and Kohno & Sofue (2024a,b). If we assume that the ^{12}CO line is optically thick, the excitation temperature is given by

$$T_{\text{ex}} = T_0^{115} \left/ \ln \left(1 + \frac{T_0^{115}}{T_{\text{B}}(^{12}\text{CO})_{\text{max}} + 0.836} \right) \right. \text{ [K]}, \quad (\text{A2})$$

where $T_{\text{B}}(^{12}\text{CO})_{\text{max}}$ corresponds to the ^{12}CO peak brightness temperature. $T_0^{115} = h\nu/k = 5.53$ K is the Planck temperature with h , ν , and k being the Planck constant, rest frequency of ^{12}CO $J = 1-0$, and Boltzmann constant, respectively. We assume that T_{ex} is equal in the ^{12}CO and ^{13}CO line emissions and express the optical depth as

$$\tau_{13} = -\ln \left(1 - \frac{T_{\text{B}}(^{13}\text{CO})_{\text{max}}/T_0^{110}}{(e^{T_0^{110}/T_{\text{ex}}} - 1)^{-1} - 0.168} \right), \quad (\text{A3})$$

where $T_{\text{B}}(^{13}\text{CO})_{\text{max}}$ and $T_0^{110} = 5.29$ K represent the ^{13}CO peak brightness temperature and the Planck temperature at the rest frequency in ^{13}CO $J = 1-0$, respectively. The ^{13}CO column density is given by

$$N_{13\text{CO}} = 3.0 \times 10^{14} \frac{\tau_{13}}{1 - e^{-\tau_{13}}} \frac{I_{13\text{CO}}}{1 - e^{-T_0^{110}/T_{\text{ex}}}} \text{ [cm}^{-2}\text{]}, \quad (\text{A4})$$

where $I_{13\text{CO}}$ is the ^{13}CO integrated intensity. Then, we convert $N_{13\text{CO}}$ to the H_2 column density using the abundance ratio of H_2 to ^{13}CO molecules given by

$$N(\text{H}_2)_{13\text{L}} = Y_{13\text{CO}} N_{13\text{CO}} \text{ [cm}^{-2}\text{]}. \quad (\text{A5})$$

Here, $Y_{13\text{CO}}$ is the abundance ratio adopted as $\sim 5 \times 10^5$ (Dickman 1978).

Finally, we derived the total molecular mass of molecular clouds from the H_2 column densities obtained by the X_{CO} and LTE method. The total molecular mass is given by

$$M = \mu_{\text{H}_2} m_{\text{H}} D^2 \sum_i \Omega N_i(\text{H}_2) \text{ [} M_{\odot}\text{]}, \quad (\text{A6})$$

where μ_{H_2} , m_{H} , D , Ω , and $N_i(\text{H}_2)$ is the mean molecular weight per hydrogen molecule of 2.8, proton mass of 1.67×10^{-24} g, distance from the solar system, solid angle, and the H_2 column density in each pixel, respectively.

REFERENCES

- Abe, D., Inoue, T., Enokiya, R., et al. 2022, ApJ, 940, 106. doi:10.3847/1538-4357/ac9e55
- Abreu-Vicente, J., Ragan, S., Kainulainen, J., et al. 2016, A&A, 590, A131. doi:10.1051/0004-6361/201527674
- Anathpindika, S. V. 2010, MNRAS, 405, 1431. doi:10.1111/j.1365-2966.2010.16541.x
- Arzoumanian, D., Russeil, D., Zavagno, A., et al. 2022, A&A, 660, A56. doi:10.1051/0004-6361/202141699
- Ascenso, J. 2018, The Birth of Star Clusters, 424, 1. doi:10.1007/978-3-319-22801-3_1
- Astropy Collaboration, Robitaille, T. P., Tollerud, E. J., et al. 2013, A&A, 558, A33
- Astropy Collaboration, Price-Whelan, A. M., Sipőcz, B. M., et al. 2018, AJ, 156, 123. doi:10.3847/1538-3881/aabc4f
- Astropy Collaboration, Price-Whelan, A. M., Lim, P. L., et al. 2022, ApJ, 935, 167. doi:10.3847/1538-4357/ac7c74
- Bains, I., Wong, T., Cunningham, M., et al. 2006, MNRAS, 367, 1609. doi:10.1111/j.1365-2966.2006.10055.x
- Becklin, E. E., Frogel, J. A., Neugebauer, G., et al. 1973, ApJL, 182, L125. doi:10.1086/181234
- Binder, B. A. & Povich, M. S. 2018, ApJ, 864, 136. doi:10.3847/1538-4357/aad7b2
- Bisbas, T. G., Tanaka, K. E. I., Tan, J. C., et al. 2017, ApJ, 850, 23. doi:10.3847/1538-4357/aa94c5
- Bonfand, M., Csengeri, T., Bontemps, S., et al. 2024, A&A, 687, A163. doi:10.1051/0004-6361/202347856
- Bolatto, A. D., Wolfire, M., & Leroy, A. K. 2013, ARA&A, 51, 207. doi:10.1146/annurev-astro-082812-140944
- Braiding, C., Burton, M. G., Blackwell, R., et al. 2015, PASA, 32, e020. doi:10.1017/pasa.2015.20
- Braiding, C., Wong, G. F., Maxted, N. I., et al. 2018, PASA, 35, e029. doi:10.1017/pasa.2018.18

- Breen, S. L., Ellingsen, S. P., Johnston-Hollitt, M., et al. 2007, *MNRAS*, 377, 491.
doi:10.1111/j.1365-2966.2007.11641.x
- Burton, M. G., Braiding, C., Glueck, C., et al. 2013, *PASA*, 30, e044. doi:10.1017/pasa.2013.22
- Chevance, M., Krumholz, M. R., McLeod, A. F., et al. 2023, *Protostars and Planets VII*, 534, 1.
doi:10.48550/arXiv.2203.09570
- Cubuk, K. O., Burton, M. G., Braiding, C., et al. 2023, *PASA*, 40, e047. doi:10.1017/pasa.2023.44
- Dedes, C., Leurini, S., Wyrowski, F., et al. 2011, *A&A*, 526, A59. doi:10.1051/0004-6361/200912874
- Dell'Ova, P., Motte, F., Gusdorf, A., et al. 2024, *A&A*, 687, A217. doi:10.1051/0004-6361/202348984
- Demachi, F., Fukui, Y., Yamada, R. I., et al. 2024, *PASJ*, 76, 1059. doi:10.1093/pasj/psae071
- Dewangan, L. K., Baug, T., & Ojha, D. K. 2020, *MNRAS*, 496, 1278. doi:10.1093/mnras/staa1526
- Dickman, R. L. 1978, *ApJS*, 37, 407. doi:10.1086/190535
- Dobbs, C. & Baba, J. 2014, *PASA*, 31, e035.
doi:10.1017/pasa.2014.31
- Dobbs, C. L., Pringle, J. E., & Duarte-Cabral, A. 2015, *MNRAS*, 446, 3608. doi:10.1093/mnras/stu2319
- Enokiya, R., Torii, K., & Fukui, Y. 2021, *PASJ*, 73, S75.
doi:10.1093/pasj/psz119
- Figuerêdo, E., Blum, R. D., Damineli, A., et al. 2005, *AJ*, 129, 1523. doi:10.1086/427394
- Fujimoto, Y., Tasker, E. J., Wakayama, M., et al. 2014, *MNRAS*, 439, 936. doi:10.1093/mnras/stu014
- Fujita, S., Torii, K., Kuno, N., et al. 2021a, *PASJ*, 73, S172.
doi:10.1093/pasj/psz028
- Fujita, S., Sano, H., Enokiya, R., et al. 2021b, *PASJ*, 73, S201. doi:10.1093/pasj/psaa078
- Fujiyoshi, T., Smith, C. H., Moore, T. J. T., et al. 1998, *MNRAS*, 296, 225. doi:10.1046/j.1365-8711.1998.01220.x
- Fujiyoshi, T., Smith, C. H., Wright, C. M., et al. 2001, *MNRAS*, 327, 233. doi:10.1046/j.1365-8711.2001.04704.x
- Fujiyoshi, T., Smith, C. H., Moore, T. J. T., et al. 2005, *MNRAS*, 356, 801. doi:10.1111/j.1365-2966.2004.08501.x
- Fujiyoshi, T., Smith, C. H., Caswell, J. L., et al. 2006, *MNRAS*, 368, 1843. doi:10.1111/j.1365-2966.2006.10255.x
- Fukui, Y., Torii, K., Hattori, Y., et al. 2018a, *ApJ*, 859, 166. doi:10.3847/1538-4357/aac217
- Fukui, Y., Kohno, M., Yokoyama, K., et al. 2018b, *PASJ*, 70, S41. doi:10.1093/pasj/psy017
- Fukui, Y., Tokuda, K., Saigo, K., et al. 2019, *ApJ*, 886, 14. doi:10.3847/1538-4357/ab4900
- Fukui, Y., Habe, A., Inoue, T., et al. 2021a, *PASJ*, 73, S1. doi:10.1093/pasj/psaa103
- Fukui, Y., Inoue, T., Hayakawa, T., et al. 2021b, *PASJ*, 73, S405. doi:10.1093/pasj/psaa079
- Galván-Madrid, R., Liu, H. B., Zhang, Z.-Y., et al. 2013, *ApJ*, 779, 121. doi:10.1088/0004-637X/779/2/121
- Gillespie, A. R., Huggins, P. J., Sollner, T. C. L. G., et al. 1977, *A&A*, 60, 221
- Grave, J. M. C., Kumar, M. S. N., Ojha, D. K., et al. 2014, *A&A*, 563, A123. doi:10.1051/0004-6361/201321306
- Griffin, M. J., Abergel, A., Abreu, A., et al. 2010, *A&A*, 518, L3
- Habe, A. & Ohta, K. 1992, *PASJ*, 44, 203
- Haworth, T. J., Tasker, E. J., Fukui, Y., et al. 2015a, *MNRAS*, 450, 10. doi:10.1093/mnras/stv639
- Haworth, T. J., Shima, K., Tasker, E. J., et al. 2015b, *MNRAS*, 454, 1634. doi:10.1093/mnras/stv2068
- Horie, S., Okamoto, T., & Habe, A. 2024, *MNRAS*, 527, 10077. doi:10.1093/mnras/stad3798
- Hunter, J. D. 2007, *Computing in Science and Engineering*, 9, 90
- Hyland, A. R., McGregor, P. J., Robinson, G., et al. 1980, *ApJ*, 241, 709. doi:10.1086/158381
- Inoue, T. & Inutsuka, S.-. ichiro . 2012, *ApJ*, 759, 35.
doi:10.1088/0004-637X/759/1/35
- Inoue, T. & Fukui, Y. 2013, *ApJL*, 774, L31.
doi:10.1088/2041-8205/774/2/L31
- Inoue, T., Hennebelle, P., Fukui, Y., et al. 2018, *PASJ*, 70, S53. doi:10.1093/pasj/psx089
- Karnik, A. D., Ghosh, S. K., Rengarajan, T. N., et al. 2001, *MNRAS*, 326, 293. doi:10.1046/j.1365-8711.2001.04596.x
- Kashiwagi, R., Iwasaki, K., & Tomisaka, K. 2023, *ApJ*, 954, 129. doi:10.3847/1538-4357/ace7bd
- Kawamura, A., Mizuno, Y., Minamidani, T., et al. 2009, *ApJS*, 184, 1. doi:10.1088/0067-0049/184/1/1
- Kinoshita, S. W. & Nakamura, F. 2022, *ApJ*, 937, 69.
doi:10.3847/1538-4357/ac8c95
- Kobayashi, M. I. N., Inutsuka, S.-. ichiro ., Kobayashi, H., et al. 2017, *ApJ*, 836, 175.
doi:10.3847/1538-4357/836/2/175
- Kobayashi, M. I. N., Kobayashi, H., Inutsuka, S.-. ichiro ., et al. 2018, *PASJ*, 70, S59. doi:10.1093/pasj/psy018
- Kobayashi, M. I. N., Iwasaki, K., Tomida, K., et al. 2023, *ApJ*, 954, 38. doi:10.3847/1538-4357/ace34e
- Koda, J., Scoville, N., & Heyer, M. 2016, *ApJ*, 823, 76.
doi:10.3847/0004-637X/823/2/76
- Kohno, M., Torii, K., Tachihara, K., et al. 2018, *PASJ*, 70, S50. doi:10.1093/pasj/psx137
- Kohno, M., Tachihara, K., Torii, K., et al. 2021, *PASJ*, 73, S129. doi:10.1093/pasj/psaa015
- Kohno, M., Nishimura, A., Fujita, S., et al. 2022, *PASJ*, 74, 24. doi:10.1093/pasj/psab107

- Kohno, M. & Sofue, Y. 2024a, *MNRAS*, 527, 9290.
doi:10.1093/mnras/stad3648
- Kohno, M. & Sofue, Y. 2024b, *PASJ*, 76, 579.
doi:10.1093/pasj/psae033
- Konishi, A., Muraoka, K., Tokuda, K., et al. 2024, *PASJ*, 76, 1098. doi:10.1093/pasj/psae073
- Krause, M. G. H., Offner, S. S. R., Charbonnel, C., et al. 2020, *SSRv*, 216, 64. doi:10.1007/s11214-020-00689-4
- Krumholz, M. R., McKee, C. F., & Bland-Hawthorn, J. 2019, *ARA&A*, 57, 227.
doi:10.1146/annurev-astro-091918-104430
- Kumar, M. S. N. 2013, *A&A*, 558, A119.
doi:10.1051/0004-6361/201321627
- Kutner, M. L. & Ulich, B. L. 1981, *ApJ*, 250, 341.
doi:10.1086/159380
- Lada, C. J. & Lada, E. A. 2003, *ARA&A*, 41, 57.
doi:10.1146/annurev.astro.41.011802.094844
- Ladd, N., Purcell, C., Wong, T., et al. 2005, *PASA*, 22, 62.
doi:10.1071/AS04068
- LHAASO Collaboration 2024, arXiv:2408.09905.
doi:10.48550/arXiv.2408.09905
- Lo, N., Cunningham, M. R., Jones, P. A., et al. 2009, *MNRAS*, 395, 1021. doi:10.1111/j.1365-2966.2009.14594.x
- Lo, N., Redman, M. P., Jones, P. A., et al. 2011, *MNRAS*, 415, 525. doi:10.1111/j.1365-2966.2011.18726.x
- Lo, N., Wiles, B., Redman, M. P., et al. 2015, *MNRAS*, 453, 3245. doi:10.1093/mnras/stv1880
- Lowe, V., Cunningham, M. R., Urquhart, J. S., et al. 2014, *MNRAS*, 441, 256. doi:10.1093/mnras/stu568
- Maity, A. K., Inoue, T., Fukui, Y., et al. 2024, *ApJ*, 974, 229. doi:10.3847/1538-4357/ad7098
- Maity, A. K., Dewangan, L. K., Bhadari, N. K., et al. 2025, *AJ*, 169, 56. doi:10.3847/1538-3881/ad98ff
- Mège, P., Russeil, D., Zavagno, A., et al. 2021, *A&A*, 646, A74. doi:10.1051/0004-6361/202038956
- Merello, M., Bronfman, L., Garay, G., et al. 2013, *ApJ*, 774, 38. doi:10.1088/0004-637X/774/1/38
- Miyawaki, R., Hayashi, M., & Hasegawa, T. 2022, *PASJ*, 74, 128. doi:10.1093/pasj/psab113
- Mizuno, A. & Fukui, Y. 2004, *Milky Way Surveys: The Structure and Evolution of our Galaxy*, 317, 59
- Moisés, A. P., Damineli, A., Figuerêdo, E., et al. 2011, *MNRAS*, 411, 705. doi:10.1111/j.1365-2966.2010.17713.x
- Molinari, S., Swinyard, B., Bally, J., et al. 2010a, *PASP*, 122, 314. doi:10.1086/651314
- Molinari, S., Swinyard, B., Bally, J., et al. 2010b, *A&A*, 518, L100. doi:10.1051/0004-6361/201014659
- Molinari, S., Schisano, E., Elia, D., et al. 2016, *A&A*, 591, A149. doi:10.1051/0004-6361/201526380
- Mookerjea, B., Kramer, C., Nielbock, M., et al. 2004, *A&A*, 426, 119. doi:10.1051/0004-6361:20040365
- Motte, F., Schilke, P., & Lis, D. C. 2003, *ApJ*, 582, 277.
doi:10.1086/344538
- Motte, F., Bontemps, S., & Louvet, F. 2018, *ARA&A*, 56, 41. doi:10.1146/annurev-astro-091916-055235
- Motte, F., Bontemps, S., Csengeri, T., et al. 2022, *A&A*, 662, A8. doi:10.1051/0004-6361/202141677
- Murase, T., Handa, T., Hirata, Y., et al. 2022, *MNRAS*, 510, 1106. doi:10.1093/mnras/stab3472
- Nguyen, H., Nguyen Lu'o'ng, Q., Martin, P. G., et al. 2015, *ApJ*, 812, 7. doi:10.1088/0004-637X/812/1/7
- Nguyen Luong, Q., Motte, F., Schuller, F., et al. 2011, *A&A*, 529, A41. doi:10.1051/0004-6361/201016271
- Nguyen-Luong, Q., Nguyen, H. V. V., Motte, F., et al. 2016, *ApJ*, 833, 23. doi:10.3847/0004-637X/833/1/23
- Nishimura, A., Ohama, A., Kimura, K., et al. 2020, *Proc. SPIE*, 11453, 114533Z. doi:10.1117/12.2562053
- Okumura, S.-I., Miyawaki, R., Sorai, K., et al. 2001, *PASJ*, 53, 793. doi:10.1093/pasj/53.5.793
- Perez, F., & Granger, B. E. 2007, *Computing in Science and Engineering*, 9, 21
- Pilbratt, G. L., Riedinger, J. R., Passvogel, T., et al. 2010, *A&A*, 518, L1. doi:10.1051/0004-6361/201014759
- Pineda, J. E., Caselli, P., & Goodman, A. A. 2008, *ApJ*, 679, 481. doi:10.1086/586883
- Pinheiro, M. C., Abraham, Z., Copetti, M. V. F., et al. 2012, *MNRAS*, 423, 2425.
doi:10.1111/j.1365-2966.2012.21049.x
- Poglitsch, A., Waelkens, C., Geis, N., et al. 2010, *A&A*, 518, L2. doi:10.1051/0004-6361/201014535
- Pouteau, Y., Motte, F., Nony, T., et al. 2023, *A&A*, 674, A76. doi:10.1051/0004-6361/202244776
- Rebolledo, D., Burton, M., Green, A., et al. 2016, *MNRAS*, 456, 2406. doi:10.1093/mnras/stv2776
- Reid, M. J., Menten, K. M., Zheng, X. W., et al. 2009, *ApJ*, 700, 137. doi:10.1088/0004-637X/700/1/137
- Reid, M. J., Menten, K. M., Brunthaler, A., et al. 2019, *ApJ*, 885, 131. doi:10.3847/1538-4357/ab4a11
- Ridge, N. A., Di Francesco, J., Kirk, H., et al. 2006, *AJ*, 131, 2921. doi:10.1086/503704
- Robitaille, T., & Bressert, E. 2012, *APLpy: Astronomical Plotting Library in Python*, ascl:1208.017
- Rodgers, A. W., Campbell, C. T., & Whiteoak, J. B. 1960, *MNRAS*, 121, 103. doi:10.1093/mnras/121.1.103
- Romano, D., Burton, M. G., Ashley, M. C. B., et al. 2019, *MNRAS*, 484, 2089. doi:10.1093/mnras/sty3510
- Russeil, D., Adami, C., Amram, P., et al. 2005, *A&A*, 429, 497. doi:10.1051/0004-6361:20048090

- Russeil, D., Tigé, J., Adami, C., et al. 2016, *A&A*, 587, A135. doi:10.1051/0004-6361/201424484
- Russeil, D., Figueira, M., Zavagno, A., et al. 2019, *A&A*, 625, A134. doi:10.1051/0004-6361/201833870
- Sakre, N., Habe, A., Pettitt, A. R., et al. 2021, *PASJ*, 73, S385. doi:10.1093/pasj/psaa059
- Sasaki, M., Robrade, J., Krause, M. G. H., et al. 2024, *A&A*, 682, A172. doi:10.1051/0004-6361/202347154
- Sault, R. J., Teuben, P. J., & Wright, M. C. H. 1995, *Astronomical Data Analysis Software and Systems IV*, 77, 433
- Shima, K., Tasker, E. J., Federrath, C., et al. 2018, *PASJ*, 70, S54. doi:10.1093/pasj/psx124
- Simpson, J. P., Cotera, A. S., Burton, M. G., et al. 2012, *MNRAS*, 419, 211. doi:10.1111/j.1365-2966.2011.19686.x
- Sofue, Y., Kohno, M., Torii, K., et al. 2019, *PASJ*, 71, S1. doi:10.1093/pasj/psy094
- Sofue, Y. & Kohno, M. 2020, *MNRAS*, 497, 1851. doi:10.1093/mnras/staa2056
- Takeuchi, T., Yamamoto, H., Torii, K., et al. 2010, *PASJ*, 62, 557. doi:10.1093/pasj/62.3.557
- Tamaoki, S., Sugitani, K., Nguyen-Luong, Q., et al. 2019, *ApJL*, 875, L16. doi:10.3847/2041-8213/ab1346
- Takahira, K., Tasker, E. J., & Habe, A. 2014, *ApJ*, 792, 63. doi:10.1088/0004-637X/792/1/63
- Takahira, K., Shima, K., Habe, A., et al. 2018, *PASJ*, 70, S58. doi:10.1093/pasj/psy011
- Tasker, E. J. 2011, *ApJ*, 730, 11. doi:10.1088/0004-637X/730/1/11
- Tasker, E. J. & Tan, J. C. 2009, *ApJ*, 700, 358. doi:10.1088/0004-637X/700/1/358
- Tokuda, K., Fukui, Y., Harada, R., et al. 2019, *ApJ*, 886, 15. doi:10.3847/1538-4357/ab48ff
- Tokuda, K., Muraoka, K., Kondo, H., et al. 2020, *ApJ*, 896, 36. doi:10.3847/1538-4357/ab8ad3
- Tokuda, K., Minami, T., Fukui, Y., et al. 2022, *ApJ*, 933, 20. doi:10.3847/1538-4357/ac6b3c
- Tokuda, K., Harada, N., Tanaka, K. E. I., et al. 2023, *ApJ*, 955, 52. doi:10.3847/1538-4357/acefb7
- Torii, K., Hattori, Y., Hasegawa, K., et al. 2017, *ApJ*, 835, 142. doi:10.3847/1538-4357/835/2/142
- Towner, A. P. M., Ginsburg, A., Dell’Ova, P., et al. 2024, *ApJ*, 960, 48. doi:10.3847/1538-4357/ad0786
- Ulich, B. L. & Haas, R. W. 1976, *ApJS*, 30, 247. doi:10.1086/190361
- van der Walt, S., Colbert, S. C., & Varoquaux, G. 2011, *Computing in Science and Engineering*, 13, 22
- Vallée, J. P. 2017, *The Astronomical Review*, 13, 113. doi:10.1080/21672857.2017.1379459
- VERA Collaboration, Hirota, T., Nagayama, T., et al. 2020, *PASJ*, 72, 50. doi:10.1093/pasj/psaa018
- Wakker, B. P. & van Woerden, H. 1997, *ARA&A*, 35, 217. doi:10.1146/annurev.astro.35.1.217
- Wiles, B., Lo, N., Redman, M. P., et al. 2016, *MNRAS*, 458, 3429. doi:10.1093/mnras/stw525
- Wong, T., Ladd, E. F., Brisbin, D., et al. 2008, *MNRAS*, 386, 1069. doi:10.1111/j.1365-2966.2008.13107.x
- Wu, B., Van Loo, S., Tan, J. C., et al. 2015, *ApJ*, 811, 56. doi:10.1088/0004-637X/811/1/56
- Yang, R.-Z. & Wang, Y. 2020, *A&A*, 640, A60. doi:10.1051/0004-6361/202037518
- Yonekura, Y., Asayama, S., Kimura, K., et al. 2005, *ApJ*, 634, 476. doi:10.1086/496869
- Zhang, M., Kainulainen, J., Mattern, M., et al. 2019, *A&A*, 622, A52. doi:10.1051/0004-6361/201732400
- Zhou, J.-W., Li, S., Liu, H.-L., et al. 2023, *MNRAS*, 519, 2391. doi:10.1093/mnras/stac3559
- Zhou, J. W., Wyrowski, F., Neupane, S., et al. 2023, *A&A*, 676, A69. doi:10.1051/0004-6361/202346500
- Zhou, J. W., Wyrowski, F., Neupane, S., et al. 2024a, *A&A*, 682, A128. doi:10.1051/0004-6361/202347377
- Zhou, J. W., Dib, S., Juvela, M., et al. 2024b, *A&A*, 686, A146. doi:10.1051/0004-6361/202449514
- Zucker, C., Battersby, C., & Goodman, A. 2018, *ApJ*, 864, 153. doi:10.3847/1538-4357/aacc66